Chlamydomonas reinhardtii triose-phosphate/phosphate translocator3 (TPT3): A major chloroplast shunt for the export of fixed carbon and reductant

Weichao Huang[a1+], Anagha Krishnan[b1], Anastasija Plett[c], Michelle Meagher[d], Nicole Linka[c], Bijie Ren[a], Justin Findinier[a], Petra Redekop[a], Neda Fakhimi[a], Jin Xu[e], Rick G. Kim[a], Devin A. Karns[b], Nanette Boyle[d], Matthew C. Posewitz[b], Arthur R. Grossman[a+]

[a]Department of Plant Biology, Carnegie Institution for Science, Stanford, CA 94305, USA

[b]Department of Chemistry and Geochemistry, Colorado School of Mines, Golden, CO 80401, USA

[c]Institute of Plant Biochemistry, Heinrich-Heine University Düsseldorf, 40225 Düsseldorf, Germany

[d]Department of Chemical and Biological Engineering, Colorado School of Mines, Golden, CO 80401, USA

[e]Department of Microbiology and Cell Science, Institute of Food and Agricultural Sciences (IFAS), University of Florida, Lake Alfred, 33885, FL, USA

[1]Authors contributed equally.

[+]Corresponding Author: Weichao Huang; Address: The Carnegie Institution for Science, 260 Panama St. Bldg. 100; Stanford, CA 94305; email: whuang@carnegiescience.edu

[+]Corresponding Author: Arthur R. Grossman; Address: The Carnegie Institution for Science, 260 Panama St. Bldg. 100; Stanford, CA 94305; email: agrossman@carnegiescience.edu

Abstract

Photosynthetic eukaryotic organisms contain several chloroplast-associated metabolite transporters that enable energetic/metabolic exchange between the chloroplast and other cellular compartments. In this study, we used the model photosynthetic alga *Chlamydomonas reinhardtii* to investigate a highly expressed chloroplast triose phosphate transporter. The triose phosphate/phosphate translocator 3 (CreTPT3), located on the Chlamydomonas chloroplast envelope, was found to be highly expressed under both non-stressed/stressed conditions (RNA level) and was characterized for substrate specificity in vitro using a yeast liposome uptake system. The CreTPT3 transporter showed high DHAP and 3-PGA transport activities, but little activity with PEP. Null mutants for CreTPT3, generated by CRISPR-Cas9 editing of the Cre*TPT*3 gene, resulted in a pleiotropic phenotype impacting photosynthetic activity, metabolite pools, carbon partitioning and storage, the redox status of the chloroplast, and the accumulation of reactive oxygen species. The results presented demonstrate that CreTPT3 is a major conduit on the chloroplast envelope for the intracellular distribution of fixed carbon and reductant generated by photosynthetic electron transport. Its function is critical for optimizing the use of resources supporting cell fitness, especially as light intensities increase, the rate of photosynthetic CO_2 fixation is elevated and the chloroplast environment becomes highly reducing.

Introduction

Photosynthetic organisms have evolved numerous strategies to distribute fixed carbon among the different cellular compartments, maintaining a dynamic metabolic/redox balance that fuels growth and biosynthetic processes. However, photosynthetic organisms can also absorb excess, potentially damaging levels of light energy during mid-day (when photosynthesis becomes saturated) and can suffer from extreme damage, especially when they experience rapid fluctuations in light intensities or are subjected to nutrient limiting conditions and other environmental stresses that impair the productive utilization of excitation energy (Chaux et al., 2017; Saroussi et al., 2017). To cope with excess excitation energy, plants and algae have evolved mechanisms to dissipate this energy through nonphotochemical quenching (NPQ), which involves both energy dependent quenching (or qE) that dissipates the energy as heat within light harvesting complexes of photosystem II (PSII), and a state transition (or qT), which results in the movement of the light harvesting antennae complexes from PSII to photosystem I (PSI) where the energy can be dissipated within the PSI reaction center. Excess reductant can also be eliminated by photochemical quenching. While the dominant form of photochemical quenching often involves the use of the electrons/reductant to fix inorganic carbon (Ci), which is used for growth or stored in the form of starch or lipids (Ge et al., 2014; Huang et al., 2018; Krishnan et al., 2015), redox equivalents can also be trafficked to other outlets where they are involved in 'nonproductive' photochemistry. The main alternative photochemical electron outlets involve the reduction of O_2 in H_2O-to-H_2O cycles that include a (*i*) Mehler-type reaction (Badger et al., 2000) that is noncatalytic and functions on the acceptor side of PSI, (*ii*) flavodiiron protein reactions (Jokel et al., 2018) (FLVs, NADPH:flavin oxidoreductase) that catalytically reduces O_2 on the acceptor side of PSI without generating reactive oxygen species (ROS), (*iii*) the plastid terminal oxidase (Houille-Vernes et al., 2011) (PTOX, plastoquinol:oxygen oxidoreductase) reaction that can use electrons of the plastoquinone (PQ) pool to reduce O_2 (thought to maintain/tune the redox state of the photosynthetic electron transport (PET) chain), and (*iv*) the movement of redox equivalents from the chloroplast to the mitochondrion where they can be used to reduce O_2 through various electron transport activities.

The extent and characteristics of metabolite and reductant shuttling between the chloroplast and other cellular compartments have not been extensively characterized despite its importance to cellular metabolism. The chloroplast is delineated by a double envelope membrane that contains

75 several metabolite translocators that are part of the machinery that governs metabolic trafficking
76 among the different cellular compartments (Facchinelli and Weber, 2011; Haferkamp and
77 Schmitz-Esser, 2012). Various mechanisms have been proposed in the shuttling of fixed carbon
78 and reducing equivalents between the chloroplast and cytoplasm. Studies with *Arabidopsis*
79 *thaliana* revealed that the malate shuttle, which involves multiple malate dehydrogenases (MDH)
80 and malate/OAA translocators (OMT), functions in the export of reductants from the chloroplast
81 and also enables the cells to manage redox conditions in the chloroplast (Zhao et al., 2018, 2020).
82 The exported malate can be used for anabolic processes or to generate NADH (during the
83 conversion of malate to oxaloacetate), which can be delivered to the mitochondrion to drive
84 oxidative phosphorylation and ATP synthesis (Zhao et al., 2020) or diverted to the mitochondrial
85 alternative oxidase pathway where it reduces O_2 to H_2O without (or with little) generation of ATP
86 (Kaye et al., 2020). The buildup of reducing equivalents in the mitochondrion or chloroplast can
87 trigger the production of ROS, which potentially activates signaling systems that modulate energy
88 metabolism and, under extreme conditions, could elicit programmed cell death (PCD) (Dietz et al.,
89 2016; Kuźniak and Kopczewski, 2020; Li and Kim, 2022; Zhao et al., 2018).

90 In addition to the malate shuttle, reduced carbon can be exported from the chloroplast by the triose
91 phosphate (triose-P)/phosphate (Pi) translocator (TPT), which can also serve potentially as a means
92 of exporting carbon from the chloroplast and a safety valve for eliminating excess reducing power
93 from the chloroplast and lessening the potential for ROS accumulation and damage (Fliege et al.,
94 1978; Flügge et al., 1989). The TPTs can potentially function as a major path for exchanging
95 metabolites between the chloroplast and cytosol. Triose-Ps are generated during photosynthetic
96 CO_2 fixation by Calvin-Benson-Bassham cycle (CBBC) activity that is supported by the reducing
97 power/energy (NADPH, ATP) derived from photosynthetic electron transport. The TPTs reside
98 on the inner chloroplast envelope membrane and can export triose-Ps, including glyceraldehyde
99 3-phosphate (G3P/GAP), dihydroxyacetone phosphate (DHAP), and 3-phosphoglycerate (3-PGA)
100 across the chloroplast envelope membrane and into the cytosol in a 1:1 counter exchange for Pi
101 (Fliege et al., 1978; Flügge et al., 1989; Lee et al., 2017a). Various plants like tobacco and
102 Arabidopsis, do not exhibit a strong phenotype if TPT is either eliminated or its level is reduced
103 (Häusler et al., 1998; Schneider et al., 2002; Walters et al., 2004). This lack of TPT activity can be
104 compensated for by moving the assimilated carbon into a transitory starch pool that is subjected to
105 accelerated turnover in the light (Häusler et al., 1998; Riesmeier et al., 1993; Walters et al., 2004),

106 leading to the production of hexoses that can be exported from the chloroplast. Characterization
107 of a double mutant (*tpt-1/adg1-1*) of Arabidopsis null for TPT (*tpt-1*) and starch synthesis (*adg1-*
108 *1*) exhibited severely compromised photosynthetic capacity and growth (Heinrichs et al., 2012;
109 Schneider et al., 2002). However, there are still few studies that demonstrate the functionalities of
110 TPT proteins in single-celled photosynthetic organisms (red algae, apicomplexans, cryptophyte)
111 by analyzing the activity of these proteins using liposome transport assays (Haferkamp et al., 2006;
112 Linka et al., 2008; Moog et al., 2020), the impact of null mutations in the gene encoding the TPT
113 on the physiology of the cells has not been investigated so far.

114 In this study, we used the unicellular green alga *Chlamydomonas reinhardtii* (Chlamydomonas
115 throughout), a well-established model organism that has been extensively used to dissect various
116 physiological processes, including photosynthesis and acclimation to environmental change.
117 Chlamydomonas contains more than 30 TPT homologs; the informatic analyses of these proteins
118 are still not refined enough to be certain of their substrate specificities and, in many cases, the
119 transported metabolite is likely not a triose-P. Here we present work that approaches the questions:
120 *i*) which of the TPTs is a triose-P/Pi translocator associated with the chloroplast envelope; *ii*) what
121 are the roles of chloroplast TPTs in partitioning carbon and reductant in cells and sustaining central
122 carbon metabolism; and finally, *iii*) do the TPTs contribute to dissipating excess reducing
123 equivalents and balancing cellular redox conditions? Our study is showing for the first time the
124 impact of *tpt* null mutations on the physiology of algal cells.

125 We have focused our analyses on Chlamydomonas TPT3 (CreTPT3) which, of the four predicted
126 chloroplast-associated CreTPTs, exhibits the strongest sequence similarity to plant chloroplast
127 TPTs and is highly expressed over the diel cycle, especially during the light period. We
128 demonstrate that CreTPT3 is located on the chloroplast envelope. Expressing CreTPT3 in yeast
129 and reconstituting it into liposomes allowed us to show that this transporter has a strong preference
130 for DHAP (dihydroxyacetone phosphate) and 3-PGA (3-phosphoglycerate) in Pi exchange assays.
131 We generated null mutants for the Cre*TPT3* gene, which exhibited growth attenuation even in low
132 light and, over the long term, were unable to survive the transition to moderate/high light. Growth,
133 along with the various other mutant phenotypes, were rescued by ectopic expression of the
134 Cre*TPT3* gene in *tpt3* mutant cells. We also examined photosynthetic performance, performed
135 metabolite analyses, measured accumulation of carbon storage products (starch and lipids), and
136 analyzed subcellular redox changes and ROS accumulation in wild type (WT) cells and the

137 Chlamydomonas *tpt3* mutant. Our results demonstrated that CreTPT3 is essential for the exchange
138 of fixed carbon, sustaining central carbon metabolism and maintaining intracellular redox balance.

139 Material and methods

140 Strains and culture conditions

141 WT Chlamydomonas M10 (CC-4403, isogenic line derived from CC-124) was used as the parental
142 strain for the generation of knockout mutants. Cultures were routinely cultivated in growth
143 chambers (LED-41L2, Percival Scientific, Inc.) at 25°C with continuous shaking on an orbital
144 shaker (VWR OS-500 Shaker) at 120 rpm, in Tris-acetate-phosphate (TAP) medium (Harris, 2009).
145 The cultures were illuminated with continuous cool white LEDs at low light (30 µmol photons m^{-}
146 ^{2} s^{-1}). Experiments were mostly performed with cells grown in the photoautotrophic medium TP
147 (TAP medium without acetate), and in TAP medium in some cases, at 25ºC, and sparged with air
148 while being shaken at 120 rpm in a growth chamber (LED-41L2, Percival Scientific, Inc.). For
149 growth assays, cultures were inoculated at a density of 0.02 at $OD_{750\ nm}$ (~1×10^{5} cells/mL) in TP
150 sparged with air under either LL or moderate light (ML, 250-300 µmol photons m^{-2} s^{-1}) intensities.

151 For spectrophotometric and chlorophyll fluorescence analyses, precultures were grown in TAP in
152 LL to mid-exponential phase, the cells were pelleted by centrifugation at 800x g, for 3 min at room
153 temperature, and the pellets were washed once with TP and then resuspended in TP at a density of
154 1-1.5 µg/mL chlorophyll. These cultures were grown in TP sparged with air and after 16-24 h in
155 LL, were transferred to ML. To avoid self-shading, the culture density was adjusted to 1-1.5 µg/mL
156 chlorophyll before ML exposure.

157 Cell samples exposed to the different light intensities were diluted to perform spot tests for
158 photoautotrophic growth on TP agar plates and for mixotrophic growth on TAP agar plates. Agar
159 plates were incubated for 7 d under either LL or ML (cool white LED) at 25°C.

160 Phylogenetic analysis

161 Protein sequences were aligned using MUSCLE (Edgar, 2004). The best-fit nucleotide substitution
162 model was generated based on the Akaike information criterion (AIC) using MEGA7 (Kumar et
163 al., 2016). Maximum likelihood phylogenetic trees were constructed based on the best-fit model
164 GTR (general time reversible) + G (gamma distribution) + I (invariable sites) with 100 bootstrap
165 replicates using MEGA7 (Kumar et al., 2016).

166

167 **Expression of CreTPT3 in yeast**

168 The DNA sequence encoding the mature CreTPT3 protein was codon-optimized for expression in
169 *Saccharomyces cerevisiae* (GeneART, ThermoFisher Scientific). This coding sequence was
170 inserted in frame with an N-terminal His tag into the yeast vector pYES-NTa (ThermoFisher
171 Scientific) using Gibson cloning (NEB). Briefly, pYES-NTa was linearized with BamHI and the
172 CreTPT3 cDNA amplified with the primer pair fwd:5'-
173 gacgataaggtacctagcGCTTCTGCTGCTGATGCTC-3' and rev:5'-
174 agaattccaccacactgTTAAGCGGCAGCTGGAGAAG-3'. This cDNA was ligated into the
175 linearized pYESS-NTa vector, which was then transformed into the yeast strain INVSc1 (MATa,
176 his3D1, leu2, trp1-289, ura3-52 / MATa, his3D1, leu2, trp1-289, and ura3-52, ThermoFisher
177 Scientific) using the lithium-acetate/PEG method (Gietz and Schiestl, 2007). Transformed yeast
178 cells were selected on synthetic complete medium containing 2% (w/v) glucose with the uracil
179 auxotrophic marker. Galactose-inducible expression of His-CreTPT3 in yeast was performed as
180 described in (Linka et al., 2008). The presence of the His-tagged fusion protein was verified by
181 standard SDS-PAGE and immunoblot analysis using an anti-His-antibody conjugated with
182 horseradish peroxidase (Miltenyi Biotech).

183 **Reconstitution into liposomes and transport activity assays**

184 For uptake studies, yeast membranes from cells with and without recombinant His-CreTPT3 were
185 enriched and reconstituted into 3% (w/v) L-alpha-phosphatidylcholine using a freeze-thaw-
186 sonication procedure (Linka et al., 2008). The reconstituted liposomes were preloaded with 30 mM
187 Pi or the indicated phosphorylated metabolites that were tested as potential transport substrates.
188 As a negative control for antiport activity, liposomes were also generated without preloading. The
189 external counter-exchange substrate was removed via gel filtration on Sephadex G-25M columns
190 (GE Healthcare). Transport assays were initiated by adding 0.25 mM [alpha-^{32}P]-phosphoric acid
191 (6,000 Ci/mmol) and performed as previously described in Linka et al. (2008). The Km for Pi was
192 determined by measuring the initial velocity at each of six external Pi concentrations between 0.05
193 and 5 mM. To obtain competitive inhibition constants (Ki), the uptake of 0.25 mM Pi into
194 liposomes containing 30 mM Pi was measured over a 4 min period in the presence of increasing
195 external inhibitor concentrations (0.05 - 5 mM). Three biological replicates were performed for all

196 described experiments. GraphPad Prism software version 9.3.0 was used for non-linear regression
197 analyses of the kinetic data.

198 **Vector construction, transformation and complementation**

199 The pRam118_VENUS plasmid which harbors the VENUS gene and the *AphVII* cassette (confers
200 resistance to hygromycin) (Cre01.g045550) (Kaye et al., 2019), was used to express Cre*TPT3*
201 (Cre01.g045550). This plasmid was linearized with HpaI (NEB). Primers: g*TPT3*_pRam118_f and
202 g*TPT3*_pRam118_r (**Supplementary Table 1**) were used to amplify Cre*TPT3* genomic DNA
203 containing an overlap with the linearized pRam118_VENUS vector. For generating the plasmid
204 pRam118-CreTPT3&VENUS, genomic DNA of Cre*TPT3* was assembled with
205 pRam118_VENUS plasmid using Gibson assembly (Gibson et al., 2009). A 1,000 bp sequence
206 upstream of Cre*TPT3* and containing the promoter region of the gene was amplified using the
207 primers TPT3pro1000_f and TPT3pro1000_r (**Supplementary Table 1**). The 3' UTR of Cre*TPT3*
208 was amplified using TPT_3UTR_f and TPT3_3UTR_r (**Supplementary Table 1**). The *PSAD*
209 promoter and the *RBCS2* 3'UTR of pRam118-CreTPT3&VENUS were replaced by the amplified
210 fragments of the 1,000 bp upstream region and the 3' UTR of Cre*TPT3*, respectively. This final
211 vector, designated pRam118_CreTPT3, contains the original Cre*TPT3* promoter (driving
212 expression of Cre*TPT3*), the genomic DNA sequence of Cre*TPT3*, VENUS and the Cre*TPT3* 3'
213 UTR plus the *AphVII* cassette. The Chlamydomonas *tpt3* mutant was transformed by
214 electroporation with 2 µg of pRam118_CreTPT3 that was linearized with AseI. The GeneArt MAX
215 Efficiency Transformation Reagent for algae (Invitrogen) was used for introducing the plasmid by
216 electroporation following the instructions provided by the manufacturer. Transformants were
217 selected on solid TAP medium containing hygromycin (10 µg/mL; Enzo Life).

218 **Subcellular localization**

219 Drug resistant transformants were visualized for VENUS fluorescence as previously described
220 (Kaye et al., 2019). In brief, transgenic cell lines resistant to hygromycin were screened for
221 VENUS fluorescence using a microplate reader (Infinite M1000; TECAN). Excitation and
222 emission settings were as follows: VENUS, excitation 515/12 nm and emission 550/12 nm;
223 chlorophyll excitation 440/9 nm and emission 680/20 nm. The TCS SP8 confocal laser-scanning
224 microscope (Leica) was used to visualize the VENUS fluorescence signal. Detailed methods for
225 visualization can be found in (Kaye et al., 2019).

226 **CRISPR-Cas9 mediated mutagenesis**

227 The protocol for disruption of Cre*TPT3* (Cre01.g045550) was adapted from (Findinier et al., 2019).
228 Chlamydomonas WT strain CC-124 was used for mutant generation. WT cells were cultured under
229 continuous light (50 µmol photons m^{-2} s^{-1}) for 2 d to a density of 3-5×10^6 cells/mL. The cells were
230 then concentrated to 2×10^8 cells/mL in 0.5×TAP supplemented with 80 mM sucrose. Two single
231 guide RNAs (sgRNA) were designed by CHOPCHOP and synthesized by Integrated DNA
232 Technologies (IDT). The sequences of the generated sgRNA are: *TPT3*-sg1 (5′-
233 CGCUGGGCGTCACUUCCCGGCGG-3′) for editing of exon 1 and *TPT3*-sg2 (5′-
234 AAGGCCGCUAUCGCCAACGUGGG-3′) for editing of exon 7. Prior to electroporation, Cas9
235 (IDT) and sgRNAs were incubated together at 37 °C for 30 min. Approximately 500 ng PCR
236 product of the *AphVII* cassette, which confers resistance to hygromycin, was added to the RNP
237 (ribonucleoprotein) mixture. 250 µl aliquots were electroporated using Super Electroporator
238 NEPA21 type II (NEPA GENE). After 16 h of recovery in very low light (10-15 µmol photons m^{-}
239 ^{2} s^{-1}), cells were plated onto solid TAP medium containing 10 µg/mL hygromycin. Sense or
240 antisense-oriented knock-ins of *AphVII* were determined by amplification using primer pairs with
241 one primer annealing to the genomic sequence and the other to the inserted sequence
242 (**Supplementary Table 1**). Amplified fragments were verified by sequencing (ELIM
243 BIOPHARM, Hayward, USA).

244 **Complementation of mutants of Cre*TPT3***

245 Mutant strains were transformed with the linearized plasmid pRam118_CreTPT3 plasmid. After
246 transformation, transformants were selected in ML and then screened for VENUS fluorescence.
247 Colonies containing VENUS and an *AphVII* cassette knock-in at the Cas9 targeted site were
248 examined for accumulation of the CreTPT3 protein by western blots using CreTPT3 antibody
249 generated by GenScript USA Inc (Piscataway, USA). Clones of Western-positive cells were
250 subjected to growth complementation assays using spot tests under ML on solid TAP or TP
251 medium.

252 **P700 activity measurements**

253 Absorbance spectroscopy for P700 analyses was performed in dark adapted liquid cultures (15
254 µg/mL chlorophyll, in 20 mM HEPES-KOH, pH 7.2, and 10% ficoll) using a JTS-100

255 spectrophotometer (SpectroLogiX, TN). Actinic light was provided by an orange LED (165 μmol
256 photons m^{-2} s^{-1}) for PSI oxidation, followed by a saturating pulse and a dark incubation. 20 μM
257 DCMU and 1 mM hydroxylamine were added to the cell suspension to inhibit linear electron flow
258 (LEF) prior to the measurement. P_{700} activity was measured by monitoring the absorbance at 705
259 nm (interference filter 6 nm FWHM was used to create a narrow excitation beam); the absorbance
260 at 740 nm was used to correct for an unspecific contribution to the 705 nm signal.

261 **Chlorophyll fluorescence analysis**

262 Chlorophyll fluorescence, used to evaluate photosynthetic electron transport, was measured using
263 a DUAL PAM-100 fluorometer. Cells were adapted in the dark for 20 min. Light curves were
264 generated by illuminating cells with increasing light intensities (0, 10, 50, 100, 200, 400, 800, 1000,
265 1200 μmol photons m^{-2} s^{-1}) for 2 min at each intensity. 1 mM CO_2 ($NaHCO_3$) was added to the
266 reaction mix as an electron receptor for the CBBC.

267 **ROS measurements and roGFP2 imaging analysis**

268 All strains were grown photoautotrophically under LL for 16-24 h. After dilution with fresh
269 medium, the cultures were transferred to ML or the dark for >48 h and then stained with CM-
270 H2DCFDA (Thermo Fisher Scientific) as described in (Kong et al., 2018) for detecting ROS.
271 Briefly, after the treatment (e.g. 48 h in ML), approximately 10 million Chlamydomonas cells
272 (treated in various ways) were pelleted and washed once with 1×PBS. The cells were then
273 resuspended in 1×PBS containing 8 μM CM-H2DCFDA and incubated at room temperature in the
274 dark for 30 min. Following this incubation, the cells were washed three times with 1×PBS buffer,
275 the fluorescent signals were either visualized using TCS SP8 confocal laser-scanning microscope
276 (Leica) or quantified with a microplate reader (Infinite M1000; TECAN). Excitation and emission
277 settings for the microscope were: 488 nm/510-530 nm HyD SMD hybrid detector for ROS, and
278 488 nm/650-700 nm-HyD SMD hybrid detector for chlorophyll autofluorescence. Excitation and
279 emission settings for the plate reader were as follows: ROS excitation 488/5 nm and emission
280 530/12 nm; chlorophyll excitation 514/5 nm and emission 690/5 nm.

281 Constructs containing chloroplast or mitochondria targeting sequences (Crozet et al., 2018) fused
282 to codon-optimized roGFP2 (Vevea et al., 2013) were transformed into WT and mutant strains.
283 Cells were cultured as shown in **Supplementary Fig. 1**. Signals from the transformed lines were

284 visualized using a TCS SP8 confocal laser-scanning microscope (Leica). Using the sequential
285 setup of the SP8, roGFP2 signals were collected at the emission wavelength of 510-550 nm upon
286 excitation of roGFP2 at 405 nm and 488 nm (Vevea et al., 2013). The degree of roGFP2 oxidation
287 was analyzed as the ratio of the emission signals after excitation at 405 nm and 488 nm (Vevea et
288 al., 2013).

289 **Photosynthesis-Irradiance curve**

290 Photosynthesis-Irradiance curves were measured using a custom Pt-Ag/AgCl polarographic
291 electrode system (ALGI) with a water jacketed (for temperature-control), 1 mL glass reaction
292 chamber. The YSI 5331A electrodes (Yellow Springs Instruments) were polarized at −0.8 V. The
293 cultures used for the assays were concentrated to 2.5-5 µg mL^{-1} chlorophyll, supplemented with
294 15 µL of 0.5 M sodium bicarbonate in water and then purged with 1% CO_2/99% He. Using a gas
295 tight syringe, the sample was transferred into the reaction chamber that was also purged with 1%
296 CO_2/99% He. The rate of change in O_2 levels was measured sequentially at the light intensities
297 100, 200, 600, 1000 µmol photons m^{-2} s^{-1} (photosynthetic active radiation, PAR); each intensity
298 was maintained for 3-5 min followed by a 3-min intervening dark period, and then the light level
299 was raised to the next higher intensity (stepped change) until the full range of intensities was tested.
300 At 1,000 µmol photons m^{-2} s^{-1}, the light was held for 10 min followed by an 8-min dark period.
301 Before the measurement of each experimental series, the electrodes were calibrated with air (~21%
302 O_2) and 1% CO_2/99% He mixture (0% O_2). The initial slope of the response was used to determine
303 the O_2 evolution rate.

304 **Starch and TAG quantification**

305 Cells were grown under LL to mid-exponential phase. Cultures were then diluted to 0.5 µg/mL
306 chlorophyll with fresh medium and transferred to and then grown in ML for 24 h or more. Starch
307 was measured using a modified method from (Klein and Betz, 1978). In brief, cells were collected
308 by centrifugation and bleached with methanol. Dried pellets were dissolved in water and heated at
309 100 ^{o}C to break the cells and release the starch. After cooling, amyloglucosidase and α-amylase
310 (2.25 U/mL) were used to hydrolyze the starch and the products of hydrolysis were quantified
311 using a Glucose Colorimetric Detection Kit (Thermo Fisher).

312 Intracellular TAG levels were estimated by a fluorometric assay using the dye Nile Red (Thermo
313 Fisher) (Yu et al., 2009). A Nile Red solution (500 µg/mL in acetone) was added to 1 mL of cell
314 suspensions at a final concentration of 0.5 µg/mL. The samples were then incubated at room
315 temperature for 30 min, and the Nile Red fluorescence emission quantified at 575 nm after
316 excitation at 530 nm using a microplate reader (Infinite M1000; TECAN).

317 **Metabolic analysis**

318 Cells grown at 30 µmol photons m^{-2} s^{-1} (LL) were shifted to 250-300 µmol photons m^{-2} s^{-1} (ML)
319 for 45 min or 6 h, as indicated. 45 mL of culture was rapidly quenched in cold saline solution (-2
320 to -3°C), extracted using cold methanol and then analyzed by LC-MS/MS. Quenching and analysis
321 of metabolites were performed according to (Sake et al., 2020) with modifications. The quenching
322 solution, filtered saline (9 g/L NaCl), was prechilled to 4ºC in a refrigerator. 30 mL of the
323 quenching solution was transferred to a 50 mL conical tube kept in an ice bath mixed with salt to
324 depress the temperature to between -3ºC and -1ºC. 15 mL of the culture was rapidly plunged into
325 the 30 mL of the quenching solution and the samples were centrifuged at 4,000 rpm for 10 min at
326 4ºC. Cell pellets were washed with fresh prechilled saline solution and centrifuged again at 4,000
327 rpm for 10 min in a 2 mL centrifuge tube. For each replicate, 45 mL of the culture was sampled
328 and the cell pellets were pooled. Washed pellets were frozen at -80ºC until extraction. Metabolite
329 extraction and further analysis were modified from (Young et al., 2011). A step-by-step protocol
330 is described in supplemental information (SI). All chemicals used for metabolite extraction and
331 LC-MS/MS analysis were Optima grade reagents.

332 **Results**

333 **Features of the triose-P/Pi translocator (TPT) family**

334 Candidate genes encoding triose-P/Pi transporters (TPT) in the Chlamydomonas genome were
335 identified by blasting the Arabidopsis TPT protein to the Chlamydomonas genome. The TPT
336 family is the largest drug/metabolite transporter (DMT) family in eukaryotes and includes triose-
337 P and sugar-phosphate permeases that are associated with chloroplasts; many family members are
338 still functionally uncharacterized (Jack et al., 2001; Knappe et al., 2003; Weber et al., 2006).
339 Chlamydomonas harbors ~32 genes encoding proteins of the TPT family, with four members
340 (CreTPT1, 2, 3 and 25) predicted to have a transit peptide and be chloroplast-localized

341 (**Supplementary Table 2**). To learn about the potential substrate specificities of the four putative
342 chloroplast CreTPTs, their amino acid sequences were aligned with the plastidial phosphate
343 transporters (PT) from Arabidopsis (AtPTs) (**Supplementary Fig. 2**).

344 Land plants harbor four classes of phosphate translocators on the inner plastid envelope, including
345 a glucose 6-phosphate transporter (GPT), a xylulose phosphate transporter (XPT), a
346 phosphoenolpyruvate transporter (PPT), and a triose-P translocator (TPT) (Eicks et al., 2002;
347 Fischer et al., 1997; Flügge et al., 1989; Kammerer et al., 1998; Lee et al., 2017b). The ability of
348 the transporters to use triose-P/DHAP or 3-PGA is dependent on five highly conserved residues
349 (H184, K203, Y338, K359, and R360 in AtTPT1) (Lee et al., 2017b; Moog et al., 2020). Only
350 CreTPT3 and CreTPT25 contain all five of these residues (H170, K189, Y322, K345, and R346
351 in CreTPT3) (**Supplementary Fig. 2**, **3**). In CreTPT2 and TPT1, H170 is replaced by N, which
352 might result in distinct substrate preferences (**Supplementary Fig. 2**, **3**). In AtTPT1, the residue
353 F262 (F248 in Chlamydomonas) is thought to inhibit phosphoenolpyruvate (PEP) access to the
354 binding site; this residue is replaced by N in AtPPT1 (PPT) (Lee et al., 2017b; Moog et al., 2020).
355 CreTPT25 has M at position F248, indicating that unlike the other CreTPTs, CreTPT25 might
356 have higher preference for PEP (**Supplementary Fig. 3**). Additionally, these findings suggest that
357 of the four chloroplast TPT family members, CreTPT3 is most likely to function in specifically
358 shuttling triose-P or 3-PGA across the chloroplast envelope.
359

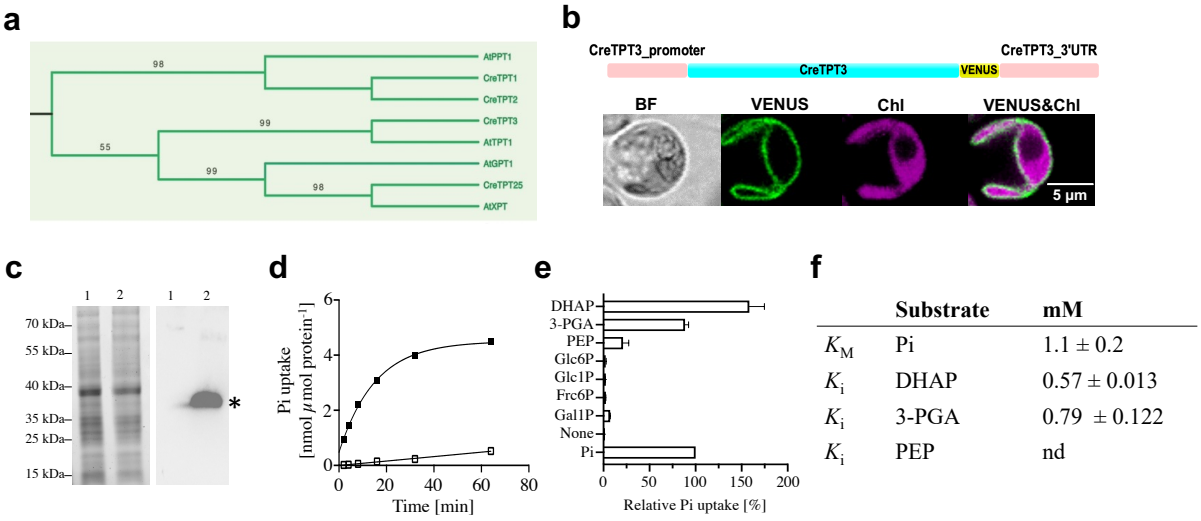

Figure 1: Chloroplast TPT phylogenies, subcellular localization of CreTPT3 and in vitro measurements of CreTPT3 transport activities. (**a**) Truncated phylogenetic tree of potential chloroplast CreTPTs. (**b**) Cellular localization of CreTPT3. The construct for expression of the CreTPT3-VENUS fusion protein is shown above the cell images and explained in the Materials and Methods. VENUS fluorescence, green; Chlorophyll (Chl) autofluorescence, magenta. (Scale bar: 5 µm). (**c**) Expression of CreTPT3 in yeast. Left, SDS-PAGE gel of proteins from total membranes isolated from yeast cells containing the empty vector (lane 1) or expressing His-CreTPT3 (lane 2). Right, corresponding immunoblot blot detection of recombinant His-CreTPT3 protein using anti-His antibodies. The calculated molecular mass of the N-terminal His-tagged protein was 37 kDa. (**d**) The kinetics of Pi exchange by His-CreTPT3 in lipid vesicles. Uptake of Pi (0.25 mM) into liposomes was measured in the presence (■) or absence (□) of Pi (30 mM) loaded within the vesicles. The arithmetic mean (±SD) of three independent experiments (each consisting of three technical replicates) was plotted with respect to the time after initiating the assay. (**e**) Analyses of substrate specificity of His-CreTPT3. Liposomes in which His-CreTPT3 was incorporated were preloaded with various substrates (30 mM) and the initial Pi uptake rates (at 0.25 mM external concentration) were determined. Relative velocities were compared to the Pi/Pi homo-exchange, which was set to 100%. The data represents the arithmetic mean (±SD) of three independent experiments (each consisting of three technical replicates). (**f**) Comparison of kinetic constants of CreTPT3. The Michaelis-Menten constant (K_M) for Pi uptake was determined using various external Pi concentrations (0.05-5 mM). The competitive inhibition constant (K_i) of Pi uptake (0.25 mM) was measured with increasing inhibitor concentrations (0.05-5 mM). Liposomes were preloaded with 30 mM Pi as the counter-exchange substrate. The data represent the arithmetic mean +/- SE of three independent experiments. ND, no competitive inhibitory constant could be measured under the given experimental conditions. DHAP, dihydroxyacetone phosphate; 3-PGA, 3-phosphoglycerate; PEP, phosphoenolpyruvate; Glc6P, glucose 6-P; Glc1P, glucose 1-P; Fru6P, fructose 6-P; Gal1P, galactose 1-P.

388 Additionally, a phylogenic tree was constructed to help determine the specificities of the putative
389 CreTPTs. This tree includes all of the CreTPTs and the plastidial phosphate transporters (PT) from
390 *Arabidopsis thaliana* (AtPPT1, AtTPT1, AtGPT1 and AtXPT1). The CreTPT1, 2, 3 and 25 protein
391 sequences cluster with the different AtTPTs (**Fig. 1a**, **Supplementary Fig 3**), again suggesting
392 that these individual Chlamydomonas transporters have different substrate specificities. Since
393 CreTPT3 is most closely related to AtTPT1 (**Fig. 1a**, **Supplementary Fig. 3**), the major triose-P
394 permease in Arabidopsis, we considered CreTPT3 as the Chlamydomonas ortholog of AtTPT1.

395 **TPT3 transport properties**

396 To help establish the physiological (in vivo) function of CreTPT3, its subcellular localization was
397 first experimentally confirmed in Chlamydomonas. The CreTPT3 coding sequence with its
398 putative chloroplast targeting sequence was fused with the VENUS tag (CreTPT3-VENUS) and
399 expressed under the control of its own promoter in the Chlamydomonas mutant null for CreTPT3.
400 As shown in **Fig. 1b**, CreTPT3-VENUS was localized to the chloroplast envelope.

401 To evaluate the substrate specificity of CreTPT3, it was heterologously expressed in
402 *Saccharomyces cerevisiae* (yeast) cells and the resulting recombinant protein was biochemically
403 analyzed using a liposome uptake system. The Cre*TPT3* gene was codon-optimized, expressed in
404 yeast (**Fig. 1c**), total cell membranes were isolated and then CreTPT3 was reconstituted into
405 liposomes (Linka et al., 2008; Loddenkötter et al., 1993). The chloroplast phosphate transporters
406 in vascular plants can catalyze a strict Pi/Pi homo-exchange in vitro. The reconstituted CreTPT3
407 in liposomes was able to catalyze the signature Pi homo-exchange, whereas in the absence of a
408 counter-exchange substrate, little Pi uptake was detected. This result demonstrates that the
409 recombinant CreTPT3 protein can function in Pi/Pi homo-exchange in liposomes (**Fig. 1d**). In
410 contrast, very low Pi uptake rates were observed for liposomes reconstituted with membranes from
411 yeast cells lacking CreTPT3 (**Supplementary Fig. 4**), indicating that the detected Pi import
412 activity was the result of CreTPT3 expression in yeast.

413 To assess the substrate specificity, the initial rates of Pi uptake into liposomes preloaded with
414 saturating concentrations (30 mM) of various putative counter-exchange substrates were
415 determined. As **Fig. 1e** shows, CreTPT3 exhibited the highest activity when DHAP was used as
416 substrate. The relative initial velocity for Pi uptake in exchange for DHAP was slightly higher than
417 that of 3-PGA (3-PGA exhibited a 75% exchange rate relative to that of Pi/DHAP) while the Pi

418 uptake into liposomes preloaded with PEP was much less efficient (about 16% relative to the
419 Pi/DHAP exchange rate) (**Fig. 1e**). Pi import was negligible when CreTPT3 liposomes were
420 preloaded with Glc-6-P, Glc-1-P, Fru-6-P, and Gal-1-P (**Fig. 1e**).

421 Characterizations of the K_M and K_i of CreTPT3 were performed to determine the affinity of the
422 transporter for the various substrates. CreTPT3 has an apparent Michaelis-Menten constant (K_M)
423 value of 1.1 +/- 0.2 mM for Pi (**Fig. 1f**), which is comparable to the value obtained for the vascular
424 plant TPT ortholog (Flügge et al., 1989). DHAP and 3-PGA competitively inhibited Pi uptake with
425 an inhibition constant (Ki) of 0.57 +/- 0.01 mM and 0.79 +/- 0.12 mM, respectively (**Fig. 1f**),
426 suggesting that CreTPT3 has a higher affinity for DHAP and 3-PGA than for Pi. In the case of
427 PEP, no inhibition of the Pi/Pi homo-exchange was observed, even at the non-physiologically high
428 concentration of 5 mM. Overall, the results of this in vitro assay indicate that CreTPT3 has a typical
429 plant-TPT substrate spectrum (Flügge et al., 1989). It can transport Pi, triose-P (DHAP) and 3-
430 PGA in a counter-exchange mode, however PEP might not be a physiologically relevant substrate
431 for CreTPT3, as was shown for apoplast TPT homologues in other organisms (Lim et al., 2010;
432 Moog et al., 2020).

433 **Isolation of *tpt3* null mutants and their impact on cell growth**

434 To explore the role of CreTPT3 in trafficking carbon and reductant across the chloroplast envelope
435 in vivo, CRISPR knockouts of Cre*TPT3* were generated. We used the CRISPR-Cas9 editing
436 system to disrupt the Cre*TPT3* gene in exons 1 and 7, while at the same time integrating the
437 hygromycin marker gene (*AphVII*) into the edited site (**Supplementary Fig. 5a**). Multiple
438 independent knockouts of Cre*TPT3* were obtained, including *t3ko1*, with the marker gene inserted
439 into exon 1, and *t3ko2* and *t3ko3*, with the marker gene inserted into exon 7 (**Supplementary Fig.
440 5**, **6**) using specific sgRNA2 guides. It was previously proposed that chloroplast TPT could
441 catalyze two potential reactions based on TPT structure analysis in red algae (Lee et al., 2017b)
442 and on in vitro assays using isolated spinach chloroplasts (Stocking and Larson, 1969): *i*) triose-P
443 (DHAP, G3P)/Pi or *ii*) triose-P /3-PGA exchange across the chloroplast inner envelope membrane.
444 The former reaction can route both carbon skeletons and reductants into the cytoplasm while
445 importing Pi back into the chloroplast for ATP regeneration. The latter reaction imports 3-PGA
446 into the chloroplast in exchange for triose-P, which allows for the export of reductant from the
447 chloroplast to the cytoplasm (DHAP or G3P), with the imported 3-PGA serving as substrate for

the CBBC, allowing for regeneration of ribulose 1,5-bisphosphate when it becomes depleted.

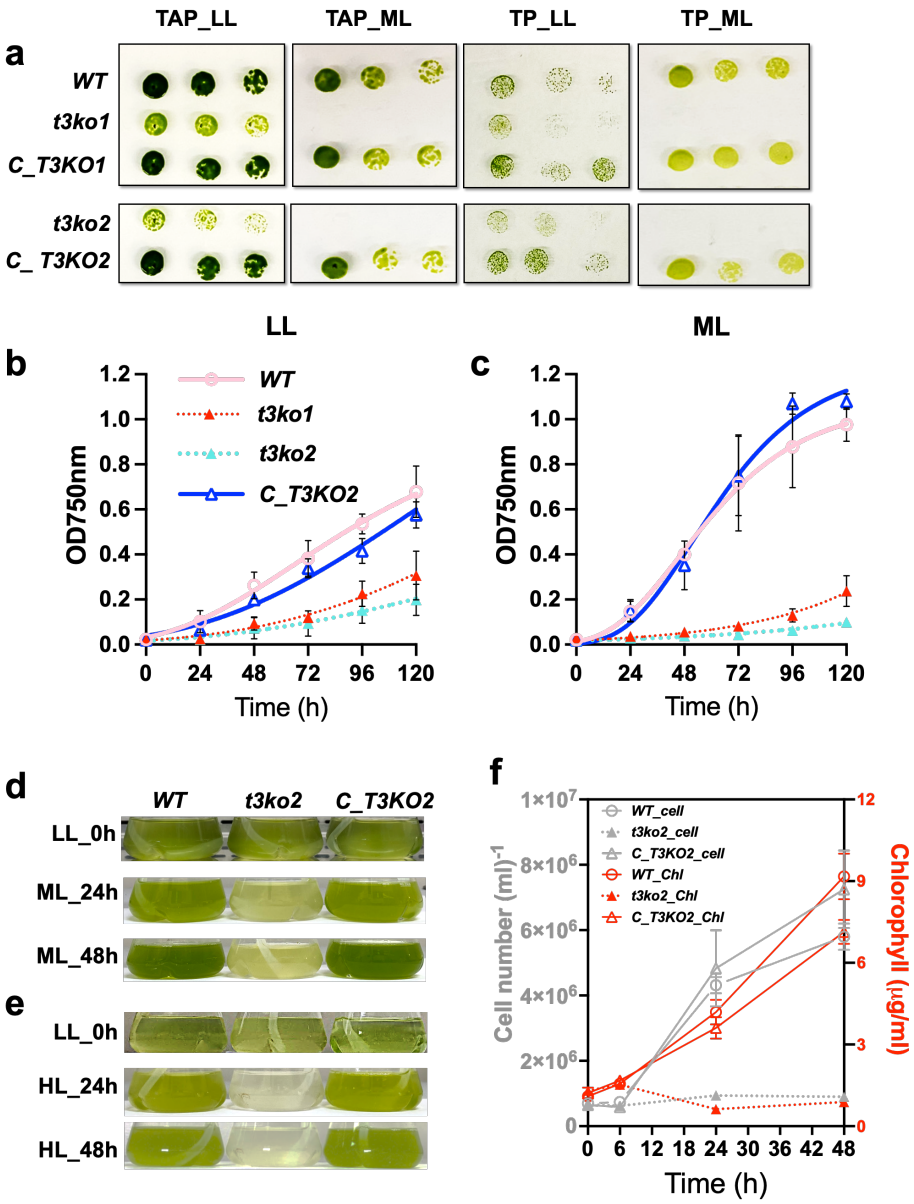

Figure 2: Growth characterization of *tpt3* mutants and complemented strains. (**a**) Growth of WT, *t3ko1*, *t3ko2* and the complemented strains (*C_T3KO1* and *C_T3KO2*, respectively), at various dilutions (see below) on agar plates incubated under low light (LL, ~30 µmol photons m^{-2} s^{-1}) and moderate light (ML, 250~300 µmol photons m^{-2} s^{-1}) for 4 days. Growth of respective strains in liquid medium under LL (**b**) and ML (**c**). The data represents the arithmetic mean (±SD) of three independent experiments. Transition of the strains from LL to ML (**d**) or to high light (HL, 450 µmol photons m^{-2} s^{-1}) (**e**) for the times indicated. (**f**) Cell growth (number) and chlorophyll content of the indicated cultures at various times following exposure to ML (from LL), for up to 48 h. In (**a**) the cells were spotted on agar plates containing TAP or TP medium under continuous

459 LL or ML conditions. The dilution series used was 1.5, 0.75, 0.375 µg/mL chlorophyll (left to
460 right). For growth in liquid medium, the cells were cultured in TP medium to an initial OD_{750nm}
461 0.02, in air and under continuous LL, before initiating the various growth analyses in LL, ML or
462 HL.

463 To elucidate the physiological roles of CreTPT3, we first examined growth of the parental WT
464 strain and the knockout mutants under either LL or ML. In contrast to WT cells, growth of the
465 Cre*TPT3* knockouts (*t3ko1*, *t3ko2*, *t3ko3*) was significantly reduced in LL on either
466 photoautotrophic (TP) or heterotrophic (TAP) agar medium (**Fig. 2a**, **Supplementary Fig. 7**),
467 while the growth of the mutant in ML was completely blocked in both TP and TAP (**Fig. 2a**).
468 Growth curves were also determined for WT and mutant cells in liquid medium (TP) in both LL
469 and ML (**Fig. 2b**, **c**); the results were in accord with those observed for the agar medium growth
470 assays. Additionally, *tpt3* mutant cells in both LL and ML exhibited an increased cell diameter and
471 formed clusters of cells that appear to be less able to separate following division **(Supplementary**
472 **Fig. 8a**, **b**). To further confirm that the growth phenotypes are a consequence of the *tpt3* knockout,
473 we introduced a wild-type copy of Cre*TPT3* fused to VENUS into the mutant strains
474 (**Supplementary Fig. 5b**). As demonstrated in **Fig. 2b** and **2c**, ectopic expression of the wild-type
475 Cre*TPT3* in the *t3ko2* mutant (*C_T3KO2*) rescued the reduced growth phenotype of the mutant in
476 both LL and ML.

477 We also analyzed the chlorophyll content of cells grown photoautotrophically upon transfer from
478 LL to ML (**Supplementary Fig. 1**) and found that *t3ko2* had reduced chlorophyll content relative
479 to WT cells after 24 h in ML (**Fig. 2d-f** and **Supplementary Fig. 9**). Cell numbers and total
480 chlorophyll were quantified following the LL to ML transition. The chlorophyll levels per cell
481 declined in all strains at 24 and 48 h following the transfer to ML; however, it was lower by more
482 than half in *t3ko2* (0.34 µg/10^6 cells) relative to either WT cells or the *C_T3KO2* rescued strain
483 (both ~0.72 µg/10^6 cells) after 24 h of ML (**Supplementary Fig. 9**), with some additional increase
484 for WT and *C_T3KO2* after 48 h of ML illumination (which might reflect some shading caused
485 by an increase in the cell density). Finally, when mutant cells were transferred HL for 24 h they
486 became highly bleached (**Fig. 2e**).

487 Taken together, these results indicate that the activity of the CreTPT3 shuttle is essential for growth
488 over a range of light intensities (LL/ML/HL).

489

490 **The *tpt3* mutant exhibits hyper-accumulation of 'storage' carbon**

491 To explore the impact of the loss of CreTPT3 activity on carbon partitioning, we quantified carbon
492 storage (starch and lipids) following a transition of WT and the *t3ko2* mutant from LL to ML.
493 Lugol staining showed extensive starch accumulation in the *t3ko2* cells after a 48-h exposure in
494 the ML, whereas, the WT cells were barely stained **(Fig. 3a)**. Furthermore, as shown in **Fig. 3b**,
495 there is an ~55-fold (WT and *t3ko2*: 13.29 and 0.24 µg starch/µg chlorophyll, respectively)
496 increase in starch accumulation (normalized to chlorophyll) in the *t3ko2* mutant after 24 h of
497 illumination in ML. The mutant also exhibited a ~24-fold (WT and *t3ko2*: 1038.93 and 41.98 Nile
498 Red fluorescence/chlorophyll, respectively) increase in lipid accumulation, as monitored by Nile
499 Red fluorescence, relative to WT and *C_T3KO2* over the same time period (**Fig. 3c, d**) (on a
500 chlorophyll basis). Since the chlorophyll in the mutant was approximately 50% relative to that of
501 WT cells after 24 h in ML, the accumulated starch and lipid on a per cell basis would be ~25-fold
502 for starch and ~12-fold for lipid in the mutant relative to the WT strains. Furthermore, the mutant
503 cells are much bigger (**Supplementary Fig. 8a, b**), which may reflect the large increase in storage
504 carbon that they accumulated in the mutant cells. Accumulated starch granules in the stroma of
505 ML-exposed *t3ko2* cells are readily visualized under bright field light microscopy
506 (**Supplementary Video 1a, b**). These results suggest that the inability to transport triose-P
507 between the chloroplast and the cytosol through CreTPT3 resulted in a repartitioning of
508 photosynthetic assimilates (carbon, reductant, and ATP) toward the synthesis of both starch and
509 TAG.

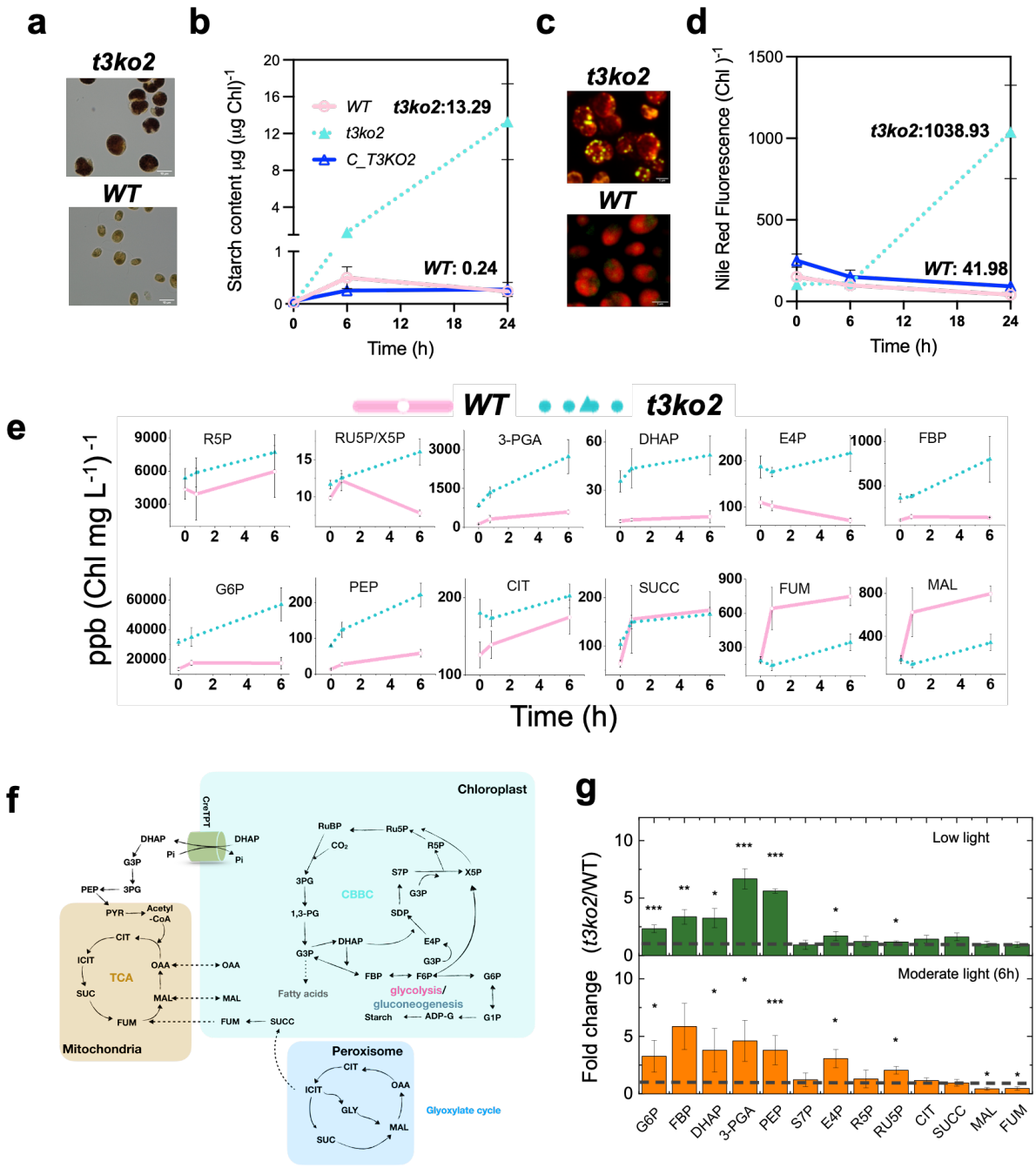

510

511 **Figure 3: Changes in storage carbon and metabolite levels in WT and *t3ko2* after**
512 **transitioning the cells from growth in LL to ML.** (**a**) Lugol staining of starch in WT and *t3ko2*
513 after 48 h of ML. (**b**) Starch content in indicated strains following 0, 6, and 24 h of ML exposure.
514 (**c**) Nile Red staining of TAG in WT and *t3ko2* following 48 h of ML exposure. (**d**) TAG content
515 in strains following 0, 6, and 24 h of ML exposure. (**e**) Time course of metabolite accumulation at
516 0 h (LL), 45 min and 6 h following ML exposure. (**f**) Select metabolic pathways in
517 Chlamydomonas; adapted from (Johnson and Alric, 2013). (**g**) Bar graph representation of fold-
518 change for metabolites shown in (**e**), calculated by dividing the pool size in *t3ko2* by that of WT

519 at the respective light levels. A fold change of 1 (no change) is shown by a dashed line. Each data
520 point shows the mean and standard error; the data represents three biological replicates for each
521 metabolite. An asterisk indicates statistically significant difference compared to WT (* P<0.05, **
522 P<0.01, *** P<0.001). Abbreviations: G6P, glucose-6-P; FBP, fructose bisphosphate; DHAP,
523 dihydroxyacetone phosphate; 3-PGA, 3-phosphoglycerate; PEP, phosphoenolpyruvate; PYR,
524 pyruvate; CIT, citrate; SUCC, succinate; FUM, fumarate; MAL, malate; E4P, Erythrose 4-P; R5P,
525 Ribose 5-P; RU5P/X5P, ribulose 5-P/xylulose-5-P.

526 **Cre*TPT3* deletion leads to accumulation of CBBC/glycolytic/gluconeogenic intermediates**

527 To understand the metabolic consequences of the loss of CreTPT3 on growth under LL and ML,
528 comparative metabolic analysis of WT and *t3ko2* mutant was performed on cells grown at LL and
529 after shifting them to ML for 45 min or 6 h. Pool sizes of various central carbon metabolites,
530 particularly those of the CBBC/glycolysis/gluconeogenesis pathways and intermediates of the
531 TCA/glyoxylate cycle (**Fig. 3f**), were quantified. Data was normalized to both chlorophyll content
532 (**Fig. 3e**) and cell number (**Supplementary Fig. 10b**). The fold-change in the quantity of each
533 metabolite in the mutant relative to WT under LL or at 45 min and 6 h after the switch to ML is
534 given in **Fig. 3g** and **Supplementary Fig. 10c**.

535 Under LL and upon transfer to ML, the *t3ko2* mutant maintained a significantly larger pool (2 to
536 6-fold) of glycolytic/gluconeogenic intermediates [DHAP, 3-PGA and FBP (all three shared with
537 CBBC), G6P, PEP], and of some metabolites of the CBBC pathway (E4P, RU5P/X5P, R5P)
538 compared to WT, suggesting that the loss of CreTPT3 results in a back-up of these metabolites
539 within the cell; our hypothesis is that they are accumulating inside the chloroplast due to the lack
540 of CreTPT3 activity. This is supported by the finding of a marked accumulation of starch and TAG
541 in the mutant strain (**Fig. 3a-d**). While the pool sizes of fumarate and malate (metabolites of the
542 TCA/glyoxylate cycle) were similar in both strains under LL, following the transition of the cells
543 to ML, WT cells showed a significant increase in the pool sizes of those metabolites while the
544 mutant maintained a lower level, indicating that the loss of CreTPT3 either directly (by supplying
545 precursors) or indirectly (metabolic rewiring) impacts their levels.

546 Thus, the one primary function of CreTPT3 would be the export of photosynthetically-synthesized
547 reduced carbon, which would drive metabolic processes in the cytoplasm and other cellular
548 compartments, while importing Pi into the chloroplast to sustain ATP synthesis.

549

550 **The *tpt3* mutant has reduced PSII activity when grown in moderate light**

551 To understand the impact of the loss of CreTPT3 activity on photosynthetic electron transport
552 (PET), we quantified photosynthetic activities following a transition from LL to ML. After
553 growing all strains photoautotrophically in LL for 16-24 h, the cultures were diluted with fresh
554 medium to a concentration of 1-1.5 µg/mL chlorophyll and then transferred to ML for 24 h
555 (**Supplementary Fig. 1**). Photosynthetic O_2 evolution rates (OERs) were measured for WT, *t3ko2*
556 and *C_T3KO2* at a range of light intensities. LL acclimated WT, *t3ko2*, and *C_T3KO2* showed
557 comparable OER at intensities below 200 µmol photons m^{-2} s^{-1} while at saturating light intensities
558 of ≥600 µmol photons m^{-2} s^{-1}, the OER of *t3ko2* was diminished relative to the WT and
559 complemented strain (**Fig. 4a**). Upon acclimation of the cells to ML for 24 h, the *t3ko2* consistently
560 displayed low OER relative to WT and *C_T3KO2* under all actinic light intensities used (**Fig. 4b**).

561 The PSII quantum yield, ΦPSII, is maximum after a dark pre-incubation (Fv/Fm). The Fv/Fm in
562 the mutant grown in LL was similar to that of WT and *C_T3KO2* immediately following the dark
563 incubation (**Fig. 4c**). The LL-acclimated WT and *t3ko2* cells exhibited comparable ΦPSII values
564 when the actinic light intensity was below 100 µmol photons m^{-2} s^{-1}, but decreased by about 20-
565 25% when the actinic light was increased to 400 µmol photons m^{-2} s^{-1}; that decrease was
566 maintained even when the actinic light was raised to over 1,000 µmol photons m^{-2} s^{-1}
567 (**Supplementary Fig. 11**). In contrast, dark acclimated mutant cells that had been exposed to ML
568 for 6 h exhibited an Fv/Fm that was about 2-fold lower than that of WT and *C_T3KO2* and
569 continued to decline over a period of 24 h in ML, with a 3-fold decrease in Fv/Fm for *t3ko2*
570 compared to that of WT (**Fig. 4c** and **Supplementary Fig. 11**).

571 The oxidation of the PQ pool is the slowest step in the PET chain between PSII and PSI (Escoubas
572 et al., 1995; Stiehl and Witt, 1969). The redox potential of the PQ pool changes upon increasing
573 the irradiance to which the cells are exposed. Thus, the redox potential of the PQ pool serves as a
574 biological measure for evaluating the balance between the photochemistry of PSII and linear
575 photosynthetic electron transport. Changes of the redox state of the PQ pool in LL and ML
576 acclimated cells were analyzed at increasing light intensities (**Fig. 4d, Supplementary Fig. 12**).
577 In LL-grown cells, the PQ pool was significantly more reduced in *t3ko2* even at low level
578 illumination (measured as 1-qL) (Saroussi et al., 2019) compared to that of WT and the rescued
579 strain. When the actinic light intensity was elevated to 400 µmol photons m^{-2} s^{-1}, the reduction

levels of the PQ pool increased for all strains, although it was still much more reduced in *t3ko2* compared to that of WT and the rescued strains (**Fig. 4d, Supplementary Fig. 12**).

For cells that had been acclimated to ML (6 h and 24 h), the PQ pool was already very highly reduced in *t3ko2* following exposure to LL, while it remained highly oxidized for both the WT and the rescued strain (**Fig. 4d, Supplementary Fig. 12**). The level of PQ reduction in ML-acclimated *t3ko2* increased only slightly with an increase in the actinic light intensity (**Fig. 4d**, **Supplementary Fig. 12**). There was also an increase in the PQ pool reduction of WT and *C_T3KO2* as the light intensity was raised, however, even at the highest light intensity the WT and rescued strains maintained a much more oxidized PQ pool than that of the mutant; the highest levels of 1-qL for WT and *C_T3KO2* were still ~2-fold lower than that of *t3ko2* (**Fig. 4d, Supplementary Fig. 12**). Overall, inactivation of CreTPT3 resulted in attenuated PSII activities (Fv/Fm, OER) and hyper-reduction of the PQ pool, suggesting a block in electron flow downstream of PQ pool.

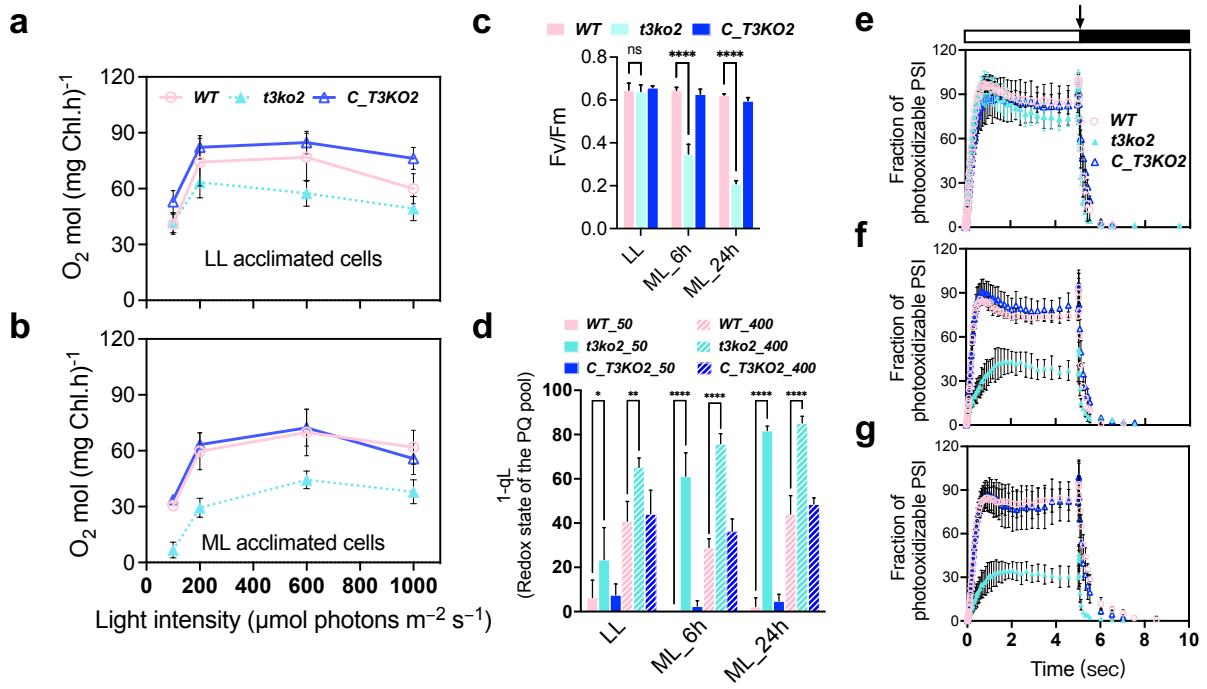

Figure 4: Photosynthetic activities followed LL to ML transition. (**a**) O_2 evolution of LL-acclimated cells in the indicated strains. (**b**) O_2 evolution of ML-acclimated (24 h) cells. (**c**) Fv/Fm of WT, *t3ko2* and the rescued strain following 6 and 24 h in ML. (**d**) 1-qL values (redox state of PQ pool) of LL- and ML-acclimated WT, *t3ko2* and the rescued strain. The acclimated cells were exposed to 50 and 400 µmol photons m^{-2} s^{-1}, as indicated, for 2 mins. (**e-g**) PSI activities following

599 a LL to ML transition. P700 oxidation and reduction kinetics in LL-grown cells (**e**) and after 6 (**f**)
600 and 24 h (**g**) in ML. Absorbance differences were monitored at 705 nm during continuous
601 illumination with 150 µmol photons·m^{-2} s^{-1} for 5 sec (white box above e), followed by a saturating
602 light pulse at 1,500 µmol photons·m^{-2} s^{-1} (arrow) and a 5 sec dark incubation (black box). The data
603 represent the arithmetic mean (±SD) of three independent experiments. Kinetics were normalized
604 by setting maximum oxidation (after light pulse) for WT to 100%. For panels c and d, the asterisks
605 represent significant differences determined by ANOVA tests. **P < 0.005, ****P < 0.0001.

606 **Impact of *tpt3* mutant on PSI activity**

607 To determine if PSI activity was also impacted in the mutant cells, we analyzed PSI/P700
608 oxidation/reduction kinetics following exposure of LL-grown cells to ML. Levels of photo-
609 oxidizable P700 were similar in all LL-acclimated strains (**Fig. 4e**). However, after 6 h in ML, the
610 level of photo-oxidizable P700 declined in the mutant to ~40% of that in WT and *C_T3KO2* cells
611 (**Fig. 4f**), followed by slightly more inhibition of PSI activity after 24 h of exposure to ML (**Fig.**
612 **4g**). These deleterious impacts on photosynthetic electron transport likely reflect a defect in routing
613 carbon/energy out of the chloroplast, which in turn will cause hyper-accumulation of reductant in
614 the chloroplast, which would potentially result a backup of PET, elevated ROS accumulation and
615 damage to the photosynthetic apparatus.

616 **CreTPT3 is crucial for balancing metabolite flux and chloroplast redox**

617 Photosynthetic organisms mainly accumulate ROS in the chloroplast and mitochondria as
618 byproducts of aerobic metabolism (Halliwell, 2006). To assay ROS production in the mutant, we
619 used the fluorescent probe CM-H2DCFDA which, upon exposure to increasing ROS levels, is
620 converted to the green fluorescent molecule dichlorofluorescein (DCF). DCF fluorescence was
621 visualized by confocal microscopy. As shown in **Fig. 5a** and **b**, ROS levels in the *t3ko2* mutant
622 were markedly increased (~3-fold) after 48 h in ML, while no difference in the level was detected
623 in WT cells.

624 For an alternative, dynamic method for evaluating redox changes in the chloroplast, we used the
625 redox sensitive green fluorescent protein roGFP2 (**Supplementary Fig. S13**) that was targeted to
626 the chloroplast stroma. Two cysteine residues were engineered into the roGFP2 to form a
627 reduction-oxidation-dependent disulfide bond that detects intracellular changes in ROS
628 accumulation (Vevea et al., 2013). roGFP2 was shown to monitor ratiometric redox changes of
629 glutathione (Dorion et al., 2021; Vevea et al., 2013). The ascorbate–glutathione (GSH) system is

630 central to ROS detoxification (Foyer and Noctor, 2011), with the redox potential of glutathione
631 reflecting ROS levels. LL-acclimated WT cells and the *t3ko2* mutant exhibited similar levels of
632 chloroplast roGFP oxidation (**Fig. 5c**). Upon transfer of WT cells to ML, the oxidation level of
633 roGFP in the chloroplast increased by ~2-fold after 1.5 h, compared to that of WT cells maintained
634 in LL, followed by a decrease after a 6 h ML exposure (**Fig. 5c**). The changes of redox in WT
635 upon a LL to ML transition is in accord with previous results (Lin et al., 2016; Vidal-Meireles et
636 al., 2017). Furthermore, the synthesis of both GSH and ascorbate increases when the redox balance
637 is shifted to a largely oxidized state after transferring cells to a higher light intensity, and recovers
638 several hours after the transfer (Lin et al., 2016; Vidal-Meireles et al., 2017) as the cells acclimate
639 to the higher light conditions. A similar redox pattern determined by chloroplast roGFP2 was
640 observed for the *t3ko2* mutant after it was shifted to ML, however, the mutant showed a much
641 greater increase in chloroplast oxidative conditions, with a 5.0-fold increase after 1.5 h, and a 2.0-
642 fold increase after 6 h, or 1.8- and 1.6-fold higher than the levels measured in WT cells (**Fig. 5c**).

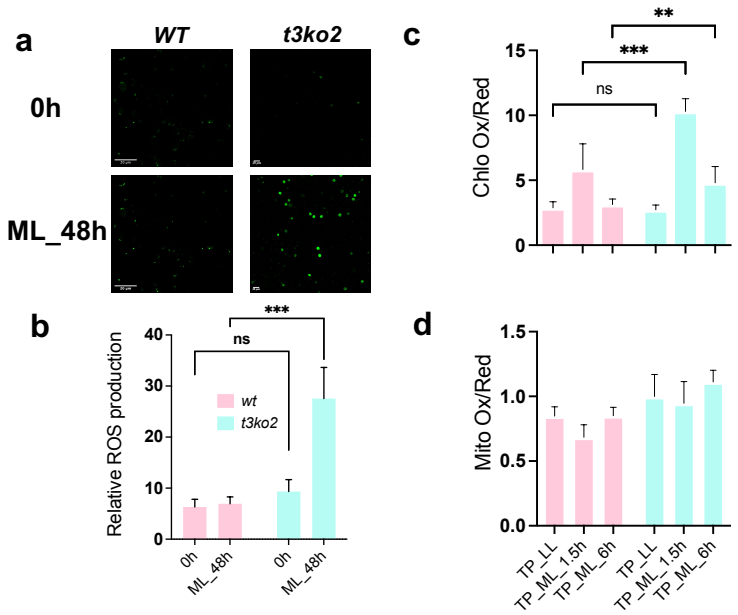

643

644 **Figure 5: Measurement of intracellular reactive ROS.** (**a**) ROS levels were evaluated by CM-
645 H2DCFDA fluorescence of WT and the *t3ko2* mutant in LL and following exposure to ML for 48
646 h. (**b**) Quantitation of data in **a**. (**c-d**) Monitoring redox levels in the chloroplast (**c**) and
647 mitochondria (**d**) after ML exposure of WT and the *t3ko2* mutant for 1.5 and 6.0 h. Values are
648 means ± SD ($n \geq 3$). The asterisks represent a significant difference determined by an ANOVA
649 test. **$P < 0.005$, ***$P < 0.001$. Strains were grown photoautotrophically under LL for 16-24 h.
650 After dilution with fresh medium, cultures were transferred to ML for the times indicated.

651 As triose-P is exported to the cytosol by CreTPT3, it could potentially donate redox equivalents to
652 mitochondrial electron transport and alter mitochondrial ROS production. Therefore, we measured
653 mitochondrial redox levels at different light intensities in both WT and the *t3ko2* mutant using the
654 roGFP sensor targeted to the mitochondrion. Upon a LL to ML transition, neither WT nor *t3ko2*
655 displayed a change in fluorescence from the mitochondrial targeted roGFP (**Fig. 5d**). These results
656 suggest that the mitochondrial redox level is maintained after shifting either LL acclimated WT or
657 *t3ko2* cells to ML. This is in agreement with the results obtained for diatoms; the roGFP oxidation
658 level in diatom mitochondria exhibited either no or minor changes in response to various stress
659 conditions, including nitrogen limitation, HL, and iron limitation (van Creveld et al., 2015).
660 Overall, these results suggest that the increase in oxidative conditions caused by a LL to ML
661 transition is primarily localized to the chloroplast in Chlamydomonas and that the inability to
662 export triose-P through TPT3 markedly increases the chloroplast oxidative stress level.

663 **Export of triose-P is essential for maintaining chloroplast redox levels in the dark**

664 Another issue that we addressed was whether CreTPT3 is important for dark metabolism in
665 Chlamydomonas. We analyzed redox changes in WT and the *t3ko2* mutant upon transferring cells
666 from LL to the dark. Intriguingly, ROS accumulation in WT was 5 times higher than that of *t3ko2*
667 after 48 h of darkness (**Fig. 6a, b**). RoGFP2 was used to determine the cellular compartment
668 associated with ROS accumulated. The oxidation level of chloroplast roGFP2 in WT was slightly
669 reduced during the first 3 h of darkness, followed by a >1.5-fold increase after 6 h of darkness
670 compared to LL-acclimated cells (**Fig. 6c**). This is in keeping with previous observations in
671 Arabidopsis in which exposing leaves to extended darkness resulted in an initial decrease in the
672 degree of oxidation of roGFP2 in the chloroplast followed by an increase to the original LL level
673 when the darkness was prolonged (Rosenwasser et al., 2011). Unlike the slight decrease in roGFP2
674 oxidation in the WT chloroplast, the oxidation state of the chloroplast in *t3ko2* cells declined by
675 2.2-fold relative to the original LL conditions and by 1.77-fold relative to WT after 3 h in the dark
676 (**Fig. 6c**). The chloroplast oxidation level in *t3ko2* did not recover to the level of WT cells after 6
677 h of darkness but attained its initial LL level after 24 h in the dark (**Fig. 6c**) suggesting that the
678 diminished export of triose-P transport and the consequent accumulation of storage carbon resulted
679 in a decline in the chloroplast redox potential in dark.

680 The initial decline in the oxidation level of the probe upon a light to dark transition indicates that

chloroplast ROS generated in the light immediately decreases after the cells are shifted to the dark. It was proposed that during an extended period in the dark, Arabidopsis becomes sugar starved which leads to the diminished availability of reductant for scavenging ROS (Rosenwasser et al., 2011; Usadel et al., 2008). Although our interpretation is speculative, given the highly reducing state of the chloroplast and the elevated accumulation of starch in the chloroplast in *t3ko2*, the mutant will likely maintain elevated levels of sugars in the chloroplast during the dark period as it mobilizes the high level of carbon stored during the light period. Indeed, as shown in **Fig. 6e**, *t3ko2* accumulates 7 times (*t3ko2*, WT: 10.21, 1.403 µg starch/µg chlorophyll) more starch than that of WT cells after 12 h in the light. Similar to WT and the rescued strain, *t3ko2* can mobilize 70% of the starch at the end of the light period (**Fig. 6e**). Thus, as the cells transition from the light to the dark, the chloroplast of *t3ko2* has approximately 7-fold more carbohydrates than that of WT cells and the rescued strain potentially giving it a greater capacity to generate metabolites that efficiently scavenge excess ROS.

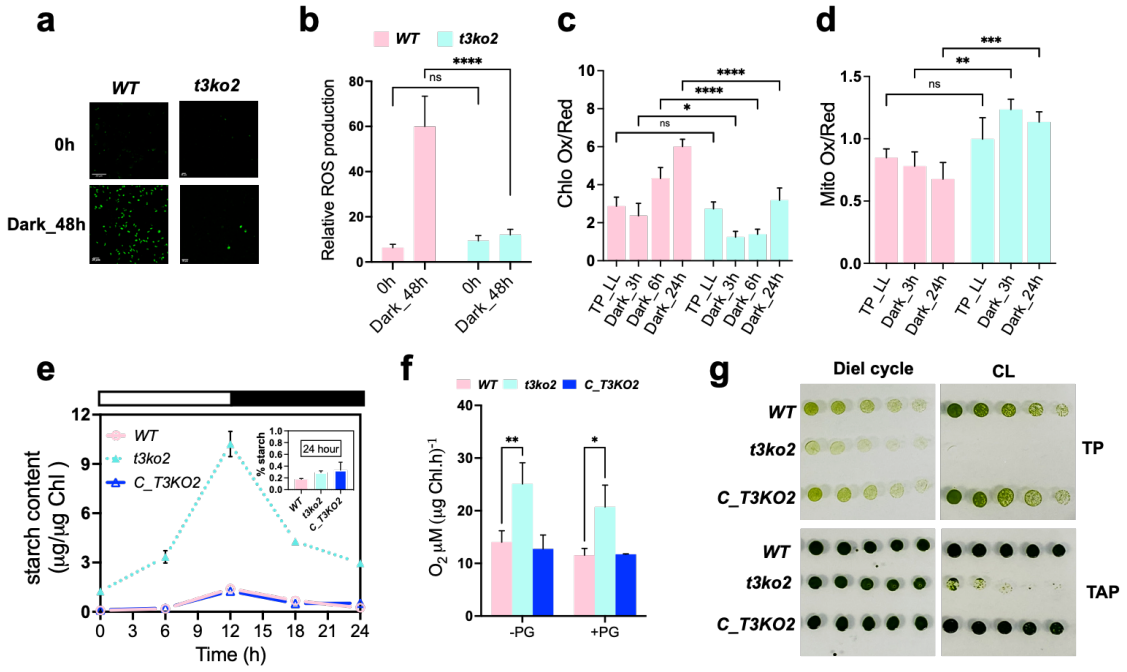

Figure 6: Metabolic and redox changes in *tpt3* over a diel cycle or extended darkness. (a) ROS levels monitored by CM-H2DCFDA staining in WT and *t3ko2* after the cells are transitioned from LL to darkness in TP medium. (**b**) Quantification of the data presented in **a**. Monitoring redox levels in the chloroplast (**c**) and mitochondrion (**d**) in the dark with roGFP2 (targeted to chloroplast and mitochondria) in WT and the *t3ko2* mutant after various times in the dark. (**e**) Starch content over the diel cycle in indicated strains. The intensity of the light phase was 60 µmol photons m^{-2}

701 s^{-1}. (**f**) Respiration during the dark phase of the diel cycle with/without *n*-propyl gallate (PG:
702 inhibitor of alternative respiration AOX+PTOX). (**g**) Growth of WT, *t3ko2* and the complemented
703 strains on agar plates in continuous light (CL) (~60 µmol photons m^{-2} s^{-1}) or on a diel cycle for 6
704 d. The cells were plated at 3, 1.5, 0.75, 0.375, and 0.1875 µg/mL chlorophyll. Values (from b,c,d,f)
705 are means ± SD (n ≥ 3). The asterisks represent significant difference determined by ANOVA. *P
706 < 0.05, **P < 0.005, ****P < 0.0001.

707 **Mitochondrial dark respiration relieves redox stress in *tpt3* mutant**

708 The mitochondrial oxidation level of *t3ko2* during the dark period was generally slightly higher
709 than that in WT (**Fig. 6d**). The respiration rate of *t3ko2* in the dark increased 2-fold compared to
710 that of WT cells irrespective of whether the mitochondrial alternative oxidase was blocked (**Fig.**
711 **6f**), suggesting that there is more substrate available for fueling mitochondrial electron flow and
712 oxidative phosphorylation, which in turn could fuel growth. These results imply that during the
713 dark period of the diel cycle, mitochondrial respiration could dissipate a proportion of the reductant
714 that accumulated in the *t3ko2* mutant during the light period. Indeed, the growth of *t3ko2* during
715 diel cycle growth (relative to continuous light) is partially rescued in TP and almost fully recovered
716 in TAP (**Fig. 6g**). In addition to growth, the morphology of *t3ko2* mutant observed over an
717 extended dark period is recovered. As shown in **Supplementary Fig. 14**, some of *t3ko2* cells are
718 aggregated under LL, however, an extended dark period results in the complete separation of *t3ko2*
719 cells. These results indicate that CreTPT3 might play only a minor role during darkness, or that
720 the loss of CreTPT3 in the dark can be compensated for by the other sugar-P transporters, such as
721 the TPT2, the putative glucose-P transporter (CreTPT25), or the maltose exporter (Findinier et al.,
722 2017). Indeed, the Cre*TPT25* and *TPT1* genes, which potentially encode the homologues of the
723 Arabidopsis glucose 6-P and phosphoenolpyruvate transporters, respectively, are upregulated in
724 darkness and downregulated in light (**Supplementary Table S3**, **Supplementary Fig. 16a**).

725 **Discussion**

726 **CreTPT3 is critical for the distribution of photosynthate**

727 Photoassimilates that serve as substrate for the chloroplast triose-P/Pi translocator (TPT) have been
728 studied in various vascular plants (e,g, tobacco, *Arabidopsis*, potato, etc). However, surprisingly
729 few studies have characterized chloroplast envelope localized members of the triose-P family in
730 trafficking fixed carbon in single-celled photosynthetic organisms (Haferkamp et al., 2006; Linka
731 et al., 2008; Moog et al., 2020); their physiological role(s) in algae has not been elucidated. In this

732 work, we hypothesized that the highly expressed Chlamydomonas chloroplast envelope triose-P/Pi
733 translocator3 (CreTPT3) functions as a 'genuine' TPT. To explore the function of CreTPT3, we
734 expressed it in yeast cells and performed in vitro studies to assay its activity in liposomes (**Fig. 1c-**
735 **f**) and also generated mutants disrupted for the Cre*TPT3* gene to examine the impact of a loss of
736 function mutant on the physiology of Chlamydomonas.

737 An Arabidopsis mutant for the chloroplast TPT was isolated 20 years ago (Schneider et al., 2002).
738 The growth and photosynthesis of this mutant, designated *ape2*, was not affected under LL
739 conditions (Walters et al., 2004), although its starch content was slightly elevated relative to that
740 of WT Arabidopsis (Walters et al., 2004). The absence of AtTPT in LL-grown plants appeared to
741 be fully compensated for by directing more photosynthate toward starch synthesis and turning over
742 the starch rapidly in the light to generate sugars like hexose phosphate (hexose-P) and other
743 metabolites that can be exported from the chloroplast. Furthermore, while *ape2* grew in HL, its
744 growth was attenuated relative to WT Arabidopsis (Walters et al., 2004), although there was no
745 detectable change in the level of starch (Schneider et al., 2002). In potato, a 2-3-fold increase in
746 starch was observed in transgenic plants with diminished levels of the chloroplast targeted TPT
747 (Riesmeier et al., 1993). The reduction in TPT activity led to a strong growth retardation during
748 the young stages of development. Similar to Arabidopsis, a tobacco strain with decreased TPT
749 activity was able to compensate for the defect by accelerating the synthesis and turnover of starch
750 and the transport of hexose from the chloroplast (Häusler et al., 1998). These observations suggest
751 that various vascular plants respond to a defect in the export of triose-P from chloroplasts by
752 moving the fixed carbon into a transient starch pool that is converted to sucrose/glucose/glucose-
753 P through accelerated hydrolysis. Glucose-P and potentially other metabolites generated from
754 starch degradation can then be exported from the chloroplast and trafficked to sink organs,
755 providing them with carbon skeletons and energy for anabolic processes (Winter and Huber, 2000).
756 In contrast, a deficiency of TPT in rice, which uses sucrose stored in leaves as its major transitory
757 form of fixed carbon rather than starch, led to reduced photosynthetic rates and about a 2-fold
758 decrease in the level of starch relative to WT plants (Lee et al., 2014).

759 The Chlamydomonas genome encodes 4 putative triose-P transporters predicted by TargetP-2.0 to
760 be routed to the chloroplast. Cre*TPT3* is the most highly expressed among the chloroplast
761 associated TPTs (**Supplementary Table S3** and **Supplementary Fig. 15a**). A detailed analysis

762 comparing Chlamydomonas TPT proteins with those of other organisms revealed that CreTPT3 is
763 most similar to the *Arabidopsis thaliana* TPT1 (**Fig. 1a**). In this study we localized CreTPT3 to
764 the chloroplast envelope. We also performed in vitro transport studies with liposomes reconstituted
765 with CreTPT3 expressed in yeast and demonstrated the capacity of this translocator to use Pi,
766 DHAP and 3-PGA as substrates (**Fig. 1d-f**), similar to the plant TPT (Flügge et al., 1989). Hence,
767 it appears that CreTPT3 can exchange chloroplast/stromal triose-Ps for cytosolic Pi, and may also
768 serve as redox shuttle by catalyzing DHAP/3-PGA exchange.

769 To probe the in vivo function of CreTPT3, we generated multiple null mutants, designated *t3ko*
770 and characterized one of the mutants (*t3ko2)* in depth. Under LL, growth of the *t3ko2* knockout
771 mutant was markedly inhibited (**Fig. 2a**, **b**, **Supplementary Fig. 7a, d**), a phenotype exacerbated
772 upon transferring the cells from LL to either ML or HL (**Fig. 2a**, **c**, **d**, **e**, **Supplementary Fig. 7b**,
773 **c**, **d**). Upon exposure to ML, *t3ko2* cells stopped growing, and when placed in HL, they exhibited
774 severe bleaching (**Fig. 2e**); this phenotype can be rescued by ectopic expression of Cre*TPT3* in the
775 mutant background. These results indicate that the flux of fixed carbon trafficked through the
776 CreTPT3 is crucial for Chlamydomonas growth under all light intensities tested, and that it
777 becomes essential for survival at the higher intensities.

778 Chlamydomonas, unlike plant cells, contains little intracellular sucrose, with starch as its major
779 form of storage carbon (Klein, 1987). In addition to a pronounced growth phenotype, the *t3ko2*
780 mutant exhibited a dramatic change in its carbon partitioning. After 24 h of LL, *t3ko2* contained
781 ~16-fold more starch than that of WT cells (**Supplementary Fig. 10a**). After 24 h in ML, the
782 starch and lipid contents of *t3ko2* were 55 and 24-fold higher than that of WT cells, respectively
783 (**Fig. 3a-d**); these results were based on normalization to chlorophyll, which was reduced by ~50%
784 in the ML-grown mutants based on the number of cells.

785 In Arabidopsis, elimination of the chloroplast targeted TPT protein did not significantly alter the
786 profiles of metabolite of either the CBBC, or the glycolytic/gluconeogenic pathways, suggesting
787 the occurrence of compensatory mechanisms that redirect carbon from the chloroplast of the
788 mutant plant (Hilgers et al., 2018). In contrast, a Chlamydomonas mutant null for Cre*TPT3*
789 exhibited a dramatic increase of most metabolites in the glycolytic/gluconeogenic pathways,
790 suggesting that triose-P exchange catalyzed by CreTPT3 was not readily compensated for by
791 alternative fixed carbon shuttles. CreTPT1, CreTPT2 and CreTPT25, the other shuttles that

792 potentially transport triose-P or hexose-P across the Chlamydomonas chloroplast envelope, are
793 unable to fully compensate for the loss of CreTPT3 (**Supplementary Fig. 15b-d**). These results
794 demonstrate the critical role of CreTPT3 in shuttling photoassimilates in Chlamydomonas. The
795 retention/accumulation of photoassimilates in the chloroplast appears to redirect them toward the
796 synthesis of starch and lipid, which would cause a marked deficit of fixed carbon in other cellular
797 compartments, such as the cytoplasm and mitochondrion, and severely compromise physiological
798 processes including cell growth and division; a loss of CreTPT3 even impacts carbon partitioning
799 and growth under various light conditions (LL/ML) as well as in the dark **(Fig. 2**, **3**, **6,**
800 **Supplementary Fig. 10**, **14**).

801 **CreTPT3 is essential for controlling 'overflow' electrons/reductant in the chloroplasts**

802 Disruption of triose-P export from the chloroplast through disruption of Cre*TPT3* also resulted in
803 inhibition of PET (**Fig. 4**). When WT, *t3ko2*, and the complemented strain *C_T3KO2* were grown
804 in LL, they exhibited a similar Fv/Fm and photosynthetic OER when exposed to low intensity
805 actinic light (**Fig. 4a**, **c**). However, even after exposure to LL, the PQ pool became more highly
806 reduced in *t3ko2* cells than in either WT or *C_T3KO2* cells (**Fig. 4d**). Hence, PSII is functioning
807 properly in LL-acclimated *t3ko2* and is capable of normal electron flow and reduction of
808 plastoquinone (PQ) to plastoquinol (plastohydroquinone, PQH2). However, reoxidation of PQH2
809 to PQ in *t3ko2* is slowed in LL-acclimated mutant cultures, which results in a decline in the rate
810 of O_2 evolution as the actinic light intensity is increased. PSI activity also appears to be unaffected
811 in LL-acclimated mutant cultures (**Fig. 4e**) which, in combination with measurements of PSII
812 activity, suggest that hyper-reduction of the PQ pool in LL-acclimated cells is caused by a block
813 in the utilization of electrons downstream of PSI. A similar hyper-reduction of the PQ pool occurs
814 when Chlamydomonas cells are unable to synthesize starch (Krishnan et al., 2015).

815 Disruption of the Cre*TPT3* gene impacted PET more acutely when the cells were transferred to
816 ML (**Fig. 4**). ML-acclimated *t3ko2* cells exhibited diminished Fv/Fm and photosynthetic OER
817 relative to WT and C_*T3KO2*. The PQ pool of ML-acclimated *t3ko2* cells was completely reduced
818 (**Fig. 4d**). Additionally, PSI activity was depressed in *t3ko2* cells transferred to ML (**Fig. 4e**).
819 These results together with the altered metabolite pool sizes and carbon partitioning in the mutant
820 (**Fig. 3**) suggest that an inability to efficiently export the terminal products of carbon fixation
821 results in hyper-reduction of the photosynthetic electron transport chain that in turn impacts the

822 activity of the photosynthetic reaction centers (PSII and PSI). The diminished Fv/Fm value in cells
823 maintained in ML clearly indicates a loss of active PSII reaction center proteins; further studies
824 will be needed to elucidate the effect of the altered metabolism on light harvesting function and
825 composition. Lower net OER may also reflect an increase in O_2 photoreduction in the light (H_2O-
826 to-H_2O cycle) in *t3ko2* mutant relative to WT cells. Future studies will focus on elucidating the
827 dynamics of O_2 evolution in this mutant using MIMS, which will help determine the importance
828 of H_2O-to-H_2O cycle in *t3ko* mutants relative to the WT cells.

829 Studies of photosynthetic activities of *t3ko2* in ML support our hypothesis that the mutant has a
830 reduced capacity to utilize reductant for anabolic processes required for growth. The ML-incubated
831 *t3ko2* mutant accumulated high levels of carbon metabolites that serve as precursors for the
832 biosynthesis of starch, lipids, and amino acids, suggesting a systems-level consequence of
833 accumulating high levels of reduced carbon in the chloroplast (**Fig. 3e**) and slowing the
834 regeneration of $NADP^+$ and ADP from NADPH and ATP, respectively. The marked alteration in
835 metabolite pools observed in the mutant could feedback on PET and potentially elicits
836 photosynthetic control, constricting electron flow at the cyt b_6f complex as a consequence of the
837 generation of a large ΔpH across the thylakoid membranes (Joliot and Johnson, 2011; Johnson and
838 Berry, 2021). Such control would result in hyper-reduction of the PQ pool and reduced electron
839 flow to PSI, which would help protect PSI from photoinhibition. Furthermore, *t3ko2* cells are
840 strongly photoinhibited following their transfer from LL to ML, conditions that cause little change
841 in PET of WT and *C_T3KO2*. These results strongly suggest that CreTPT3 is essential for
842 maintaining the flow of fixed carbon and reductant from the chloroplast to the cytosol where it can
843 be allocated for various anabolic processes that support normal cell growth.

844 The malate-OAA shunt was shown to play a role in exporting reductant from chloroplasts and
845 linking chloroplast redox stress, which can be elicited by high light and various conditions that
846 limit growth and/or block photosynthetic activities, to mitochondrial metabolism (Zhao et al.,
847 2020). The malate-OAA shunt represents another activity that, under high redox stress, might have
848 compensated for the loss of the CreTPT3 shuttle. Intriguingly, malate levels in *t3ko2* were 4-fold
849 lower than in WT cells following a transition from LL to ML (**Fig. 3e**, **g**). Furthermore, a previous
850 study of metabolic flux analysis during heterotrophic growth of Chlamydomonas showed that the
851 TPT shuttle is almost 10-fold more active than the malate-OAA shunt (Boyle et al., 2017). These

852 results together with the physiological phenotypes of the *tpt3ko* mutant suggest that the malate-
853 OAA shunt cannot compensate for a loss of CreTPT3 activity. Furthermore, Cre*TPT3* is the most
854 responsive/upregulated of the four Chlamydomonas, chloroplast-localized *TPT* genes following
855 exposure of cells to nitrogen, sulfur or iron deprivation (**Supplementary Fig. 16 b-d**), suggesting
856 that it plays an important role in controlling chloroplast redox conditions. Deprivation of
857 Chlamydomonas for nitrogen or sulfur caused dramatic attenuation of PET (Saroussi et al., 2017)
858 as the cells elicited an array of 'energy management' strategies to balance energy generation and
859 utilization (Saroussi et al., 2017). Elevated NPQ, chlororespiration and lipid/starch accumulation
860 are well recognized mechanisms to dissipate excess light energy and minimize ROS production in
861 Chlamydomonas in response to nutrient deprivation (Saroussi et al., 2017). In this study, TPT3-
862 dependent chloroplast triose-P/Pi transport appears to be critical for distributing fixed carbon and
863 reductant to other cellular compartments. When this function is compromised, the chloroplast
864 accumulates various metabolites and altered substrate availability for chloroplast-localized
865 metabolic processes; elevated $NADPH/NADP^+$ and ATP/ADP^+ ratios, hyper-reduction of
866 chloroplast redox components, such as the PQ pool, and elevated production of ROS can lead to
867 dysfunction of the photosynthetic apparatus (and other metabolic activities).

868 **CreTPT3 is central to metabolic and redox networks**

869 AGPase, a key enzyme in starch synthesis, is exquisitely sensitive to allosteric regulation; it is
870 activated by 3-PGA and inhibited by Pi (Preiss, 1988). When the *t3ko2* mutant was exposed to LL,
871 there was already a dramatic increase of 3-PGA (6-fold) relative to WT cells (**Fig. 3e**, **g**). The loss
872 of CreTPT3 might also lead to less import of Pi into chloroplasts. Therefore, the ratio of 3-PGA/Pi
873 would be markedly elevated in the *tpt3* mutant compared to that of the WT cells and the
874 complemented strain. Thus, even in LL, AGPase in the mutant would become active, which in turn
875 would lead to starch accumulation (**Supplementary Fig. 10a**).

876 In chloroplasts, reductant generated by photosynthetic electron transport can modulate the activity
877 of various redox-sensitive target proteins via thiol-based redox regulation. Key metabolic
878 pathways both within and external to the chloroplast must be coordinated with the rate at which
879 the photosynthetic light reactions produce reductant and ATP (Cejudo et al., 2021; Yoshida and
880 Hisabori, 2018; Yu et al., 2020). Chloroplasts harbor two thiol-based redox systems that
881 independently regulate plastid metabolism by communicating redox conditions to specific target

882 enzymes, thereby increasing or decreasing their activities. One system, FDX/TRX reductase,
883 obtains reducing equivalents from FDX (which is reduced by PET) (Meyer et al., 2008) while the
884 other involves NADPH-TRX reductase (NTRC), which uses NADPH as its substrate (Pérez-Ruiz
885 and Cejudo, 2009). Both systems can activate ADP-glucose pyrophosphorylase (AGPase) and
886 starch biosynthesis (Ballicora et al., 2000; Lepistö et al., 2013). There was a dramatic impact of
887 the loss of CreTPT3 on the redox state of PET components. Illumination of LL-acclimated *t3ko2*
888 mutant cells with 50 µmol photons m^{-2} s^{-1} actinic light resulted in elevated reduction of the PQ
889 pool compared to that of WT (**Fig. 4d**) while exposure of the mutant to ML for 6 h led to near
890 complete reduction of the PQ pool (**Fig. 4d**, **Supplementary Fig. 12**), which could activate the
891 FDX/TRX system and alter the activities of its various target enzymes, including increasing
892 AGPase activity, which is needed for the synthesis of starch. Furthermore, an increase in the levels
893 of phosphorylated intermediates of the CBBC (**Fig. 3e**, **g**) typically leads to a reduced rate of
894 cycling NADPH to $NADP^+$, resulting in a higher NADPH:$NADP^+$ ratio and availability of
895 reductant for activation of the NTRC (NADPH-TRX reductase) system, which would also
896 contribute to AGPase activation and starch hyperaccumulation.

897 In sum, we show that the loss of a chloroplast envelope localized triose-P/Pi exchange protein
898 results in elevated 3-PGA levels and slow turnover of carbon precursors and reducing equivalents,
899 leading to PET hyper-reduction. This could possibly result in an increase in the NADPH:$NADP^+$
900 ratio. These metabolic alterations would lead to both allosteric (high 3-PGA) and redox regulated
901 (Trx or NTRC systems) activation of AGPase, even in LL. Hence, starch overaccumulation in
902 *t3ko2* would initially reflect metabolic control, with subsequent regulation through the FDX/TRX
903 or NTRC redox system (see model on **Fig. 7**).

904 Additionally, the highly compromised transport of triose-P out of the chloroplast in *t3ko2* would
905 lead to hyper-reduction of photosynthetic electron carriers, which is reflected by a highly reduced
906 PQ pool, the redox state of the chloroplast and mitochondrion obtained by roGFP analyses, and
907 elevated ROS production/accumulation (**Fig. 5a-c**). ROS was initially considered harmful, causing
908 oxidative stress, damaging lipids, proteins, and DNA, eventually resulting in cell death (Schieber
909 and Chandel, 2014). Increasing evidence, however, suggests that low levels of ROS can function
910 in diverse signaling pathways (Schieber and Chandel, 2014) that regulate various cellular
911 processes (Foyer and Noctor, 2005; Wagner et al., 2004) such as growth, the cell cycle, senescence

912 (Zimmermann and Zentgraf, 2005), and acclimation to stressful biotic and abiotic conditions
913 (Miller et al., 2008). ROS can also regulate expression of some chloroplast genes encoding proteins
914 associated with photosynthesis and modulation of PET (Yu et al., 2020). For example, ROS
915 inhibits *de novo* synthesis of the PSII reaction center protein D1, which would lead to
916 photoinhibition during high light acclimation (Kojima et al., 2007; Nishiyama et al., 2001).
917 Moreover, when PSI becomes highly reduced, superoxide and singlet oxygen both elicit PSI
918 photoinhibition (Takagi et al., 2016).

919 Overall, Chlamydomonas mutants lacking TPT3 develop a hyper-reduced chloroplast landscape
920 with elevated ROS production (**Fig. 5c**). After 6 h or more in ML, PSII and PSI activities in the
921 mutant become compromised, most likely a consequence of elevated ROS levels (see model on
922 **Fig. 7**). The chloroplast generated ROS serves as a messenger for reporting redox information (e.g.
923 light levels, stress conditions) to the regulatory machinery of the cell, which results in modulation
924 of expression of nuclear genes that would ameliorate the impact and damage associated with
925 elevated ROS levels (Exposito-Rodriguez et al., 2017; Foyer, 2018; Wakao and Niyogi, 2021).
926 Many studies have shown that stress-induced lipid/triacylglycerol (TAG) accumulation also
927 correlates with an increase in ROS production (Shi et al., 2017); ROS may activate diacylglycerol
928 acyltransferases (DGAT) and phospholipid diacylglycerol acyltransferase activities (PDAT)
929 thereby stimulating lipid accumulation (Chouhan et al., 2021).

930 As depicted in **Fig. 7**, we propose that various tiers of redox regulation are responsible for the
931 differential physiological responses of the Chlamydomonas *tpt3* knockout mutants relative to WT
932 cells and the rescued strain. When *t3ko2* cells are initially transferred from LL to ML, the triose-P
933 pool and metabolites derived from that pool accumulate in the mutant because of its reduced
934 capacity to move triose-P out of the chloroplast, which also causes reduced CBBC activity, hyper-
935 reduction of PET and the accumulation of ROS (which would inhibit photosynthetic activity). The
936 hyper-reduction and accumulation of fixed carbon in the chloroplast of the *tpt3* mutants would
937 activate AGPase through allosteric regulation and the FDX/TRX and the NTRC redox systems,
938 leading to starch hyper-accumulation (**Fig. 7**). Furthermore, increased ROS/RS accumulation and
939 the elevated redox state of PET would elicit retrograde signals that mediate changes in expression
940 of both chloroplast and nuclear genes, marshaling the synthesis of specific activities that function
941 to ameliorate the impact of the hyper-reduced state of the chloroplast resulting from the

compromised ability of the cells to export reductant and fixed carbon from the organelle (**Fig. 7**).

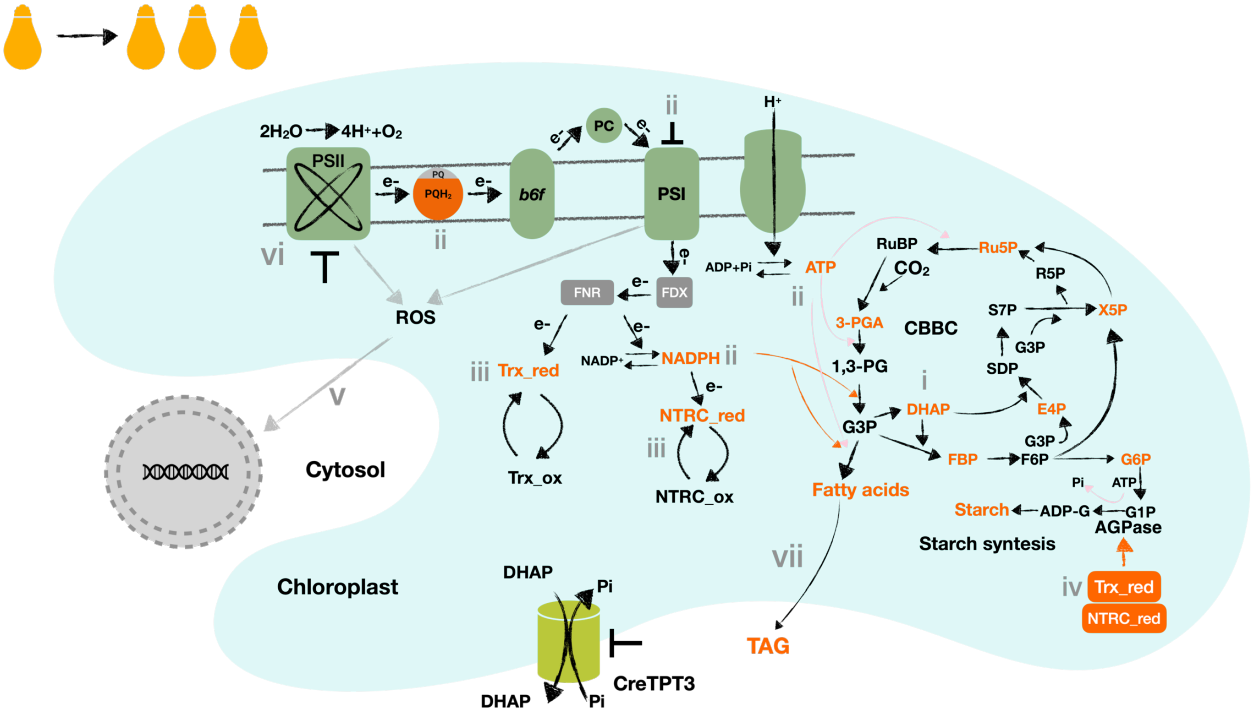

Figure 7: Impact of eliminating Chlamydomonas TPT3 on the chloroplast metabolic landscape. i. reduced triose-P export leads to accumulation of sugar-P (e.g. triose-P, hexose-P, marked in pink), and an elevated ratio of 3-PGA/Pi (which can activate AGPase activity) would stimulate production of storage carbon; CBBC activity diminishes along with the fixation of CO_2, leading to hyperaccumulation of reductant (NADPH) and energy (ATP) within the chloroplast; **ii.** the elevated NADPH:NADP$^+$ and ATP:ADP ratios, elicit strong feedback on PET causing hyper-reduction of electron carriers (eg: over reduced PQ pool and highly reduced PSI) that slows electron flow across the cytochrome *b₆f* complex; **iii.** the highly reduced PET system and the elevated NADPH can actively reduce FDX/TRX and the NTRC, respectively; **iv.** reduced TRX and/or NTRC can activate the AGPase (above the activity elicited by an increase in the 3-PGA/Pi ratio), leading to additional starch accumulation; **v.** hyper-reduction of PET can also lead to ROS accumulation; **vi.** ROS can act as a signal that controls expression of chloroplast and nuclear genes; **vii.** ROS also cause damage to both PSII and I and lead to lipid accumulation as a consequence of activation of diacylglycerol acyltransferases (DGAT) and phospholipid diacylglycerol acyltransferase (PDAT). Many of these metabolic/acclimatory processes both overlap and are interconnected. Under conditions of extended exposure to moderate light, the damage in the Chlamydomonas *tpt3* mutant can accumulate and lead to cell death; cell death occurs rapidly in high light.

963 **Acknowledgments:**

964 WH thanks M. Onishi for advice on generation of CRISPR mutants and A. Burlacot for help with
965 PQ pool measurements.

966 **Fundings:**

967 This project has received funding from DOE award DE-SC0019417. RGK and JF were supported
968 by the Department of Plant Biology of the Carnegie Institution for Science. PR was supported by
969 Human Frontier Science Program (HFSP) RGP0046/2018 (to ARG).

970 **Author contributions**

971 WH, AK, ARG and MP conceptualized the study. WH generated the CRISPR mutants as well as
972 the complemented strain, localized the TPT3 protein, analyzed the redox status in the cell,
973 performed respiration measurements, measured the reduction level of PQ pool, analyzed changes
974 of starch over the diel cycle. AK performed the experiments of photosynthetic O_2 evolution,
975 extraction of samples for LC-MS/MS, data analysis of LC-MS/MS. AP and NL performed the
976 reconstitution into liposomes and transport activity assays. MM and NB performed LC-MS/MS
977 and analyses of metabolite data. BR performed data mining for transcriptome and the Nile red
978 staining. JF and NF analyzed starch changes upon transition from LL to ML. WH, PR and ARG
979 analyzed PSI and PSII activities. JF and BR constructed roGFP2 associated vectors. JX and WH
980 performed the phylogenetic tree. WH drafted the manuscript. ARG, MP, AK, NL, NB, AP, MM
981 and all the other authors helped with revising and finalizing the manuscript.

982

983 **References**

984 Badger, M.R., von Caemmerer, S., Ruuska, S., and Nakano, H. (2000). Electron flow to oxygen
985 in higher plants and algae: rates and control of direct photoreduction (Mehler reaction) and rubisco
986 oxygenase. Philos. Trans. R. Soc. Lond. B Biol. Sci. *355*, 1433–1446.
987 https://doi.org/10.1098/rstb.2000.0704.

988 Ballicora, M.A., Frueauf, J.B., Fu, Y., Schürmann, P., and Preiss, J. (2000). Activation of the
989 potato tuber ADP-glucose pyrophosphorylase by thioredoxin. J. Biol. Chem. *275*, 1315–1320.
990 https://doi.org/10.1074/jbc.275.2.1315.

991 Boyle, N.R., Sengupta, N., and Morgan, J.A. (2017). Metabolic flux analysis of heterotrophic
992 growth in *Chlamydomonas reinhardtii*. PLoS One *12*, e0177292.
993 https://doi.org/10.1371/journal.pone.0177292.

994 Cejudo, F.J., González, M.-C., and Pérez-Ruiz, J.M. (2021). Redox regulation of chloroplast
995 metabolism. Plant Physiol. *186*, 9–21. https://doi.org/10.1093/plphys/kiaa062.

996 Chaux, F., Burlacot, A., Mekhalfi, M., Auroy, P., Blangy, S., Richaud, P., and Peltier, G. (2017).
997 Flavodiiron Proteins Promote Fast and Transient O_2 Photoreduction in Chlamydomonas. Plant
998 Physiol. *174*, 1825–1836. https://doi.org/10.1104/pp.17.00421.

999 Chouhan, N., Devadasu, E., Yadav, R.M., and Subramanyam, R. (2021). Autophagy induced
1000 accumulation of lipids in *pgrl1* and *pgr5* of *Chlamydomonas reinhardtii* under high light. Front.
1001 Plant Sci. *12*, 752634. https://doi.org/10.3389/fpls.2021.752634.

1002 van Creveld, S.G., Rosenwasser, S., Schatz, D., Koren, I., and Vardi, A. (2015). Early perturbation
1003 in mitochondria redox homeostasis in response to environmental stress predicts cell fate in diatoms.
1004 ISME J. *9*, 385–395. https://doi.org/10.1038/ismej.2014.136.

1005 Crozet, P., Navarro, F.J., Willmund, F., Mehrshahi, P., Bakowski, K., Lauersen, K.J., Pérez-Pérez,
1006 M.-E., Auroy, P., Gorchs Rovira, A., Sauret-Gueto, S., et al. (2018). Birth of a Photosynthetic
1007 Chassis: A MoClo Toolkit Enabling Synthetic Biology in the Microalga *Chlamydomonas*
1008 *reinhardtii*. ACS Synth. Biol. *7*, 2074–2086. https://doi.org/10.1021/acssynbio.8b00251.

1009 Dietz, K.-J., Turkan, I., and Krieger-Liszkay, A. (2016). Redox- and Reactive Oxygen Species-
1010 Dependent Signaling into and out of the Photosynthesizing Chloroplast. Plant Physiol. *171*, 1541–
1011 1550. https://doi.org/10.1104/pp.16.00375.

1012 Dorion, S., Ouellet, J.C., and Rivoal, J. (2021). Glutathione Metabolism in Plants under Stress:
1013 Beyond Reactive Oxygen Species Detoxification. Metabolites *11*, 641.
1014 https://doi.org/10.3390/metabo11090641.

1015 Edgar, R.C. (2004). MUSCLE: multiple sequence alignment with high accuracy and high
1016 throughput. Nucleic Acids Res. *32*, 1792–1797. https://doi.org/10.1093/nar/gkh340.

1017 Eicks, M., Maurino, V., Knappe, S., Flügge, U.-I., and Fischer, K. (2002). The plastidic pentose
1018 phosphate translocator represents a link between the cytosolic and the plastidic pentose phosphate

1019 pathways in plants. Plant Physiol. *128*, 512–522. https://doi.org/10.1104/pp.010576.

1020 Escoubas, J.M., Lomas, M., LaRoche, J., and Falkowski, P.G. (1995). Light intensity regulation
1021 of cab gene transcription is signaled by the redox state of the plastoquinone pool. Proc. Natl. Acad.
1022 Sci. U. S. A. *92*, 10237–10241. https://doi.org/10.1073/pnas.92.22.10237.

1023 Exposito-Rodriguez, M., Laissue, P.P., Yvon-Durocher, G., Smirnoff, N., and Mullineaux, P.M.
1024 (2017). Photosynthesis-dependent H_2O_2 transfer from chloroplasts to nuclei provides a high-light
1025 signalling mechanism. Nat. Commun. *8*. https://doi.org/10.1038/s41467-017-00074-w.

1026 Facchinelli, F., and Weber, A.P.M. (2011). The metabolite transporters of the plastid envelope: an
1027 update. Front. Plant Sci. *2*, 50. https://doi.org/10.3389/fpls.2011.00050.

1028 Findinier, J., Tunçay, H., Schulz-Raffelt, M., Deschamps, P., Spriet, C., Lacroix, J.-M., Duchêne,
1029 T., Szydlowski, N., Li-Beisson, Y., Peltier, G., et al. (2017). The Chlamydomonas *mex1* mutant
1030 shows impaired starch mobilization without maltose accumulation. J. Exp. Bot. *68*, 5177–5189.
1031 https://doi.org/10.1093/jxb/erx343.

1032 Findinier, J., Delevoye, C., and Cohen, M.M. (2019). The dynamin-like protein Fzl promotes
1033 thylakoid fusion and resistance to light stress in *Chlamydomonas reinhardtii*. PLoS Genet. *15*,
1034 e1008047. https://doi.org/10.1371/journal.pgen.1008047.

1035 Fischer, K., Kammerer, B., Gutensohn, M., Arbinger, B., Weber, A., Hausler, R.E., and Flugge,
1036 U.-I. (1997). A new class of plastidic phosphate translocators: A putative link between primary
1037 and secondary metabolism by the phosphoenolpyruvate/phosphate antiporter. Plant Cell *9*, 453.
1038 https://doi.org/10.2307/3870494.

1039 Fliege, R., Flügge, U.-I., Werdan, K., and Heldt, H.W. (1978). Specific transport of inorganic
1040 phosphate, 3-phosphoglycerate and triosephosphates across the inner membrane of the envelope
1041 in spinach chloroplasts. Biochim. Biophys. Acta Bioenerg. *502*, 232–247.
1042 https://doi.org/10.1016/0005-2728(78)90045-2.

1043 Flügge, U.I., Fischer, K., Gross, A., Sebald, W., Lottspeich, F., and Eckerskorn, C. (1989). The
1044 triose phosphate-3-phosphoglycerate-phosphate translocator from spinach chloroplasts:
1045 nucleotide sequence of a full-length cDNA clone and import of the in vitro synthesized precursor
1046 protein into chloroplasts. EMBO J. *8*, 39–46. .

1047 Foyer, C.H. (2018). Reactive oxygen species, oxidative signaling and the regulation of
1048 photosynthesis. Environ. Exp. Bot. *154*, 134–142.
1049 https://doi.org/10.1016/j.envexpbot.2018.05.003.

1050 Foyer, C.H., and Noctor, G. (2005). Redox Homeostasis and Antioxidant Signaling: A Metabolic
1051 Interface between Stress Perception and Physiological Responses. Plant Cell *17*, 1866–1875.
1052 https://doi.org/10.1105/tpc.105.033589.

1053 Foyer, C.H., and Noctor, G. (2011). Ascorbate and glutathione: the heart of the redox hub. Plant
1054 Physiol. *155*, 2–18. https://doi.org/10.1104/pp.110.167569.

1055 Ge, F., Huang, W., Chen, Z., Zhang, C., Xiong, Q., Bowler, C., Yang, J., Xu, J., and Hu, H. (2014).
1056 Methylcrotonyl-CoA Carboxylase Regulates Triacylglycerol Accumulation in the Model Diatom
1057 *Phaeodactylum tricornutum*. Plant Cell *26*, 1681–1697. https://doi.org/10.1105/tpc.114.124982.

1058 Gibson, D.G., Young, L., Chuang, R.-Y., Venter, J.C., Hutchison, C.A., 3rd, and Smith, H.O.
1059 (2009). Enzymatic assembly of DNA molecules up to several hundred kilobases. Nat. Methods *6*,
1060 343–345. https://doi.org/10.1038/nmeth.1318.

1061 Gietz, R.D., and Schiestl, R.H. (2007). High-efficiency yeast transformation using the LiAc/SS
1062 carrier DNA/PEG method. Nat. Protoc. *2*, 31–34. https://doi.org/10.1038/nprot.2007.13.

1063 Haferkamp, I., and Schmitz-Esser, S. (2012). The plant mitochondrial carrier family: functional
1064 and evolutionary aspects. Front. Plant Sci. *3*, 2. https://doi.org/10.3389/fpls.2012.00002.

1065 Haferkamp, I., Deschamps, P., Ast, M., Jeblick, W., Maier, U., Ball, S., and Neuhaus, H.E. (2006).
1066 Molecular and biochemical analysis of periplastidial starch metabolism in the cryptophyte
1067 Guillardia theta. Eukaryot. Cell *5*, 964–971. https://doi.org/10.1128/EC.00381-05.

1068 Halliwell, B. (2006). Reactive species and antioxidants. Redox biology is a fundamental theme of
1069 aerobic life. Plant Physiol. *141*, 312–322. https://doi.org/10.1104/pp.106.077073.

1070 Harris, E.H. (2009). Chlamydomonas sourcebook: Introduction to Chlamydomonas and its
1071 laboratory use (Academic Press).

1072 Häusler, R.E., Schlieben, N.H., Schulz, B., and Flügge, U.I. (1998). Compensation of decreased
1073 triose phosphate/phosphate translocator activity by accelerated starch turnover and glucose
1074 transport in transgenic tobacco. Planta *204*, 366–376. https://doi.org/10.1007/s004250050268.

1075 Heinrichs, L., Schmitz, J., Flügge, U.-I., and Häusler, R.E. (2012). The Mysterious Rescue of
1076 adg1-1/tpt-2 - an Arabidopsis thaliana Double Mutant Impaired in Acclimation to High Light - by
1077 Exogenously Supplied Sugars. Front. Plant Sci. *3*, 265. https://doi.org/10.3389/fpls.2012.00265.

1078 Hilgers, E.J.A., Schöttler, M.A., Mettler-Altmann, T., Krueger, S., Dörmann, P., Eicks, M., Flügge,
1079 U.-I., and Häusler, R.E. (2018). The Combined Loss of Triose Phosphate and Xylulose 5-
1080 Phosphate/Phosphate Translocators Leads to Severe Growth Retardation and Impaired
1081 Photosynthesis in *Arabidopsis thaliana* tpt/xpt Double Mutants. Front. Plant Sci. *9*, 1331.
1082 https://doi.org/10.3389/fpls.2018.01331.

1083 Houille-Vernes, L., Rappaport, F., Wollman, F.-A., Alric, J., and Johnson, X. (2011). Plastid
1084 terminal oxidase 2 (PTOX2) is the major oxidase involved in chlororespiration in Chlamydomonas.
1085 Proc. Natl. Acad. Sci. U. S. A. *108*, 20820–20825. https://doi.org/10.1073/pnas.1110518109.

1086 Huang, W., Haferkamp, I., Lepetit, B., Molchanova, M., Hou, S., Jeblick, W., Río Bártulos, C.,
1087 and Kroth, P.G. (2018). Reduced vacuolar β-1,3-glucan synthesis affects carbohydrate metabolism
1088 as well as plastid homeostasis and structure in *Phaeodactylum tricornutum*. Proc. Natl. Acad. Sci.
1089 U. S. A. *115*, 4791–4796. https://doi.org/10.1073/pnas.1719274115.

1090 Jack, D.L., Yang, N.M., and Saier, M.H., Jr (2001). The drug/metabolite transporter superfamily.

1091 Eur. J. Biochem. *268*, 3620–3639. https://doi.org/10.1046/j.1432-1327.2001.02265.x.

1092 Johnson, X., and Alric, J. (2013). Central carbon metabolism and electron transport in
1093 *Chlamydomonas reinhardtii*: metabolic constraints for carbon partitioning between oil and starch.
1094 Eukaryot. Cell *12*, 776–793. https://doi.org/10.1128/EC.00318-12.

1095 Jokel, M., Johnson, X., Peltier, G., Aro, E.-M., and Allahverdiyeva, Y. (2018). Hunting the main
1096 player enabling *Chlamydomonas reinhardtii* growth under fluctuating light. Plant J. *94*, 822–835.
1097 https://doi.org/10.1111/tpj.13897.

1098 Kammerer, B., Fischer, K., Hilpert, B., Schubert, S., Gutensohn, M., Weber, A., and Flügge, U.I.
1099 (1998). Molecular characterization of a carbon transporter in plastids from heterotrophic tissues:
1100 the glucose 6-phosphate/phosphate antiporter. Plant Cell *10*, 105–117.
1101 https://doi.org/10.1105/tpc.10.1.105.

1102 Kaye, Y., Huang, W., Clowez, S., Saroussi, S., Idoine, A., Sanz-Luque, E., and Grossman, A.R.
1103 (2019). The mitochondrial alternative oxidase from *Chlamydomonas reinhardtii* enables survival
1104 in high light. J. Biol. Chem. *294*, 1380–1395. https://doi.org/10.1074/jbc.RA118.004667.

1105 Klein, U. (1987). Intracellular Carbon Partitioning in *Chlamydomonas reinhardtii*. Plant Physiol.
1106 *85*, 892–897. https://doi.org/10.1104/pp.85.4.892.

1107 Klein, U., and Betz, A. (1978). Fermentative metabolism of hydrogen-evolving *Chlamydomonas*
1108 *moewusii*. Plant Physiol. *61*, 953–956. https://doi.org/10.1104/pp.61.6.953.

1109 Knappe, S., Flügge, U.-I., and Fischer, K. (2003). Analysis of the plastidic phosphate translocator
1110 gene family in Arabidopsis and identification of new phosphate translocator-homologous
1111 transporters, classified by their putative substrate-binding site. Plant Physiol. *131*, 1178–1190.
1112 https://doi.org/10.1104/pp.016519.

1113 Kojima, K., Oshita, M., Nanjo, Y., Kasai, K., Tozawa, Y., Hayashi, H., and Nishiyama, Y. (2007).
1114 Oxidation of elongation factor G inhibits the synthesis of the D1 protein of photosystem II. Mol.
1115 Microbiol. *65*, 936–947. https://doi.org/10.1111/j.1365-2958.2007.05836.x.

1116 Kong, F., Burlacot, A., Liang, Y., Légeret, B., Alseekh, S., Brotman, Y., Fernie, A.R., Krieger-
1117 Liszkay, A., Beisson, F., Peltier, G., et al. (2018). Interorganelle Communication: Peroxisomal
1118 MALATE DEHYDROGENASE2 Connects Lipid Catabolism to Photosynthesis through Redox
1119 Coupling in Chlamydomonas. Plant Cell *30*, 1824–1847. https://doi.org/10.1105/tpc.18.00361.

1120 Krishnan, A., Kumaraswamy, G.K., Vinyard, D.J., Gu, H., Ananyev, G., Posewitz, M.C., and
1121 Dismukes, G.C. (2015). Metabolic and photosynthetic consequences of blocking starch
1122 biosynthesis in the green alga *Chlamydomonas reinhardtii* sta6 mutant. Plant J. *81*, 947–960.
1123 https://doi.org/10.1111/tpj.12783.

1124 Kumar, S., Stecher, G., and Tamura, K. (2016). MEGA7: Molecular Evolutionary Genetics
1125 Analysis version 7.0 for bigger datasets. Mol. Biol. Evol. *33*, 1870–1874.
1126 https://doi.org/10.1093/molbev/msw054.

1127 Kuźniak, E., and Kopczewski, T. (2020). The chloroplast reactive oxygen species-redox system in
1128 plant immunity and disease. Front. Plant Sci. *11*, 572686.
1129 https://doi.org/10.3389/fpls.2020.572686.

1130 Lee, S.-K., Eom, J.-S., Voll, L.M., Prasch, C.M., Park, Y.-I., Hahn, T.-R., Ha, S.-H., An, G., and
1131 Jeon, J.-S. (2014). Analysis of a triose phosphate/phosphate translocator-deficient mutant reveals
1132 a limited capacity for starch synthesis in rice leaves. Mol. Plant *7*, 1705–1708.
1133 https://doi.org/10.1093/mp/ssu082.

1134 Lee, Y., Nishizawa, T., Takemoto, M., Kumazaki, K., Yamashita, K., Hirata, K., Minoda, A.,
1135 Nagatoishi, S., Tsumoto, K., Ishitani, R., et al. (2017a). Crystal structure of the triose-
1136 phosphate/phosphate translocator in complex with inorganic phosphate.
1137 https://doi.org/10.2210/pdb5y78/pdb.

1138 Lee, Y., Nishizawa, T., Takemoto, M., Kumazaki, K., Yamashita, K., Hirata, K., Minoda, A.,
1139 Nagatoishi, S., Tsumoto, K., Ishitani, R., et al. (2017b). Structure of the triose-
1140 phosphate/phosphate translocator reveals the basis of substrate specificity. Nat Plants *3*, 825–832.
1141 https://doi.org/10.1038/s41477-017-0022-8.

1142 Lepistö, A., Pakula, E., Toivola, J., Krieger-Liszkay, A., Vignols, F., and Rintamäki, E. (2013).
1143 Deletion of chloroplast NADPH-dependent thioredoxin reductase results in inability to regulate
1144 starch synthesis and causes stunted growth under short-day photoperiods. J. Exp. Bot. *64*, 3843–
1145 3854. https://doi.org/10.1093/jxb/ert216.

1146 Li, M., and Kim, C. (2022). Chloroplast ROS and stress signaling. Plant Commun *3*, 100264.
1147 https://doi.org/10.1016/j.xplc.2021.100264.

1148 Lim, L., Linka, M., Mullin, K.A., Weber, A.P.M., and McFadden, G.I. (2010). The carbon and
1149 energy sources of the non-photosynthetic plastid in the malaria parasite. FEBS Lett. *584*, 549–554.
1150 https://doi.org/10.1016/j.febslet.2009.11.097.

1151 Lin, S.-T., Chiou, C.-W., Chu, Y.-L., Hsiao, Y., Tseng, Y.-F., Chen, Y.-C., Chen, H.-J., Chang,
1152 H.-Y., and Lee, T.-M. (2016). Enhanced Ascorbate Regeneration Via Dehydroascorbate Reductase
1153 Confers Tolerance to Photo-Oxidative Stress in *Chlamydomonas reinhardtii*. Plant Cell Physiol.
1154 *57*, 2104–2121. https://doi.org/10.1093/pcp/pcw129.

1155 Linka, M., Jamai, A., and Weber, A.P.M. (2008). Functional characterization of the plastidic
1156 phosphate translocator gene family from the thermo-acidophilic red alga *Galdieria sulphuraria*
1157 reveals specific adaptations of primary carbon partitioning in green plants and red algae. Plant
1158 Physiol. *148*, 1487–1496. https://doi.org/10.1104/pp.108.129478.

1159 Loddenkötter, B., Kammerer, B., Fischer, K., and Flügge, U.I. (1993). Expression of the functional
1160 mature chloroplast triose phosphate translocator in yeast internal membranes and purification of
1161 the histidine-tagged protein by a single metal-affinity chromatography step. Proc. Natl. Acad. Sci.
1162 U. S. A. *90*, 2155–2159. https://doi.org/10.1073/pnas.90.6.2155.

1163 Meyer, Y., Siala, W., Bashandy, T., Riondet, C., Vignols, F., and Reichheld, J.P. (2008).
1164 Glutaredoxins and thioredoxins in plants. Biochim. Biophys. Acta *1783*, 589–600.

1165 https://doi.org/10.1016/j.bbamcr.2007.10.017.

1166 Miller, G., Shulaev, V., and Mittler, R. (2008). Reactive oxygen signaling and abiotic stress.
1167 Physiol. Plant. *133*, 481–489. https://doi.org/10.1111/j.1399-3054.2008.01090.x.

1168 Moog, D., Nozawa, A., Tozawa, Y., and Kamikawa, R. (2020). Substrate specificity of plastid
1169 phosphate transporters in a non-photosynthetic diatom and its implication in evolution of red alga-
1170 derived complex plastids. Sci. Rep. *10*, 1167. https://doi.org/10.1038/s41598-020-58082-8.

1171 Nishiyama, Y., Yamamoto, H., Allakhverdiev, S.I., Inaba, M., Yokota, A., and Murata, N. (2001).
1172 Oxidative stress inhibits the repair of photodamage to the photosynthetic machinery. EMBO J. *20*,
1173 5587–5594. https://doi.org/10.1093/emboj/20.20.5587.

1174 Pérez-Ruiz, J.M., and Cejudo, F.J. (2009). A proposed reaction mechanism for rice NADPH
1175 thioredoxin reductase C, an enzyme with protein disulfide reductase activity. FEBS Lett. *583*,
1176 1399–1402. https://doi.org/10.1016/j.febslet.2009.03.067.

1177 Preiss, J. (1988). Biosynthesis of starch and its regulation. In The Biochemistry of Plants,
1178 (Elsevier), pp. 181–254.

1179 Riesmeier, J.W., Flügge, U.I., Schulz, B., Heineke, D., Heldt, H.W., Willmitzer, L., and Frommer,
1180 W.B. (1993). Antisense repression of the chloroplast triose phosphate translocator affects carbon
1181 partitioning in transgenic potato plants. Proc. Natl. Acad. Sci. U. S. A. *90*, 6160–6164.
1182 https://doi.org/10.1073/pnas.90.13.6160.

1183 Rosenwasser, S., Rot, I., Sollner, E., Meyer, A.J., Smith, Y., Leviatan, N., Fluhr, R., and Friedman,
1184 H. (2011). Organelles contribute differentially to reactive oxygen species-related events during
1185 extended darkness. Plant Physiol. *156*, 185–201. https://doi.org/10.1104/pp.110.169797.

1186 Sake, C.L., Newman, D.M., and Boyle, N.R. (2020). Evaluation of quenching methods for
1187 metabolite recovery in photoautotrophic *Synechococcus sp*. PCC 7002. Biotechnol. Prog. *36*,
1188 e3015. https://doi.org/10.1002/btpr.3015.

1189 Saroussi, S., Sanz-Luque, E., Kim, R.G., and Grossman, A.R. (2017). Nutrient scavenging and
1190 energy management: acclimation responses in nitrogen and sulfur deprived Chlamydomonas. Curr.
1191 Opin. Plant Biol. *39*, 114–122. https://doi.org/10.1016/j.pbi.2017.06.002.

1192 Schieber, M., and Chandel, N.S. (2014). ROS function in redox signaling and oxidative stress.
1193 Curr. Biol. *24*, R453-62. https://doi.org/10.1016/j.cub.2014.03.034.

1194 Schneider, A., Häusler, R.E., Kolukisaoglu, Ü., Kunze, R., Van der Graaff, E., Schwacke, R.,
1195 Catoni, E., Desimone, M., and Flügge, U.I. (2002). An Arabidopsis thaliana knock-out mutant of
1196 the chloroplast triose phosphate/phosphate translocator is severely compromised only when starch
1197 synthesis, but not starch mobilisation is abolished. Plant Journal https://doi.org/10.1046/j.1365-
1198 313X.2002.01460.x.

1199 Shi, K., Gao, Z., Shi, T.-Q., Song, P., Ren, L.-J., Huang, H., and Ji, X.-J. (2017). Reactive oxygen
1200 species-mediated cellular stress response and lipid accumulation in oleaginous microorganisms:

The state of the art and future perspectives. Front. Microbiol. *8*, 793. https://doi.org/10.3389/fmicb.2017.00793.

Stiehl, H.H., and Witt, H.T. (1969). Quantitative Treatment of the Function of Plastoquinone in Photosynthesis. Zeitschrift Für Naturforschung B *24*, 1588–1598. https://doi.org/10.1515/znb-1969-1219.

Stocking, C.R., and Larson, S. (1969). A chloroplast cytoplasmic shuttle and the reduction of extraplastid NAD. Biochem. Biophys. Res. Commun. *37*, 278–282. https://doi.org/10.1016/0006-291x(69)90731-1.

Takagi, D., Takumi, S., Hashiguchi, M., Sejima, T., and Miyake, C. (2016). Superoxide and singlet oxygen produced within the thylakoid membranes both cause photosystem I photoinhibition. Plant Physiol. *171*, 1626–1634. https://doi.org/10.1104/pp.16.00246.

Usadel, B., Bläsing, O.E., Gibon, Y., Retzlaff, K., Höhne, M., Günther, M., and Stitt, M. (2008). Global transcript levels respond to small changes of the carbon status during progressive exhaustion of carbohydrates in Arabidopsis rosettes. Plant Physiol. *146*, 1834–1861. https://doi.org/10.1104/pp.107.115592.

Vevea, J.D., Alessi Wolken, D.M., Swayne, T.C., White, A.B., and Pon, L.A. (2013). Ratiometric biosensors that measure mitochondrial redox state and ATP in living yeast cells. J. Vis. Exp. 50633. https://doi.org/10.3791/50633.

Vidal-Meireles, A., Neupert, J., Zsigmond, L., Rosado-Souza, L., Kovács, L., Nagy, V., Galambos, A., Fernie, A.R., Bock, R., and Tóth, S.Z. (2017). Regulation of ascorbate biosynthesis in green algae has evolved to enable rapid stress-induced response via the VTC2 gene encoding GDP-l-galactose phosphorylase. New Phytol. *214*, 668–681. https://doi.org/10.1111/nph.14425.

Wagner, D., Przybyla, D., den Camp, R. op, Kim, C., Landgraf, F., Lee, K.P., Würsch, M., Laloi, C., Nater, M., Hideg, E., et al. (2004). The Genetic Basis of Singlet Oxygen–Induced Stress Responses of *Arabidopsis thaliana*. Science https://doi.org/10.1126/science.1103178.

Wakao, S., and Niyogi, K.K. (2021). Chlamydomonas as a model for reactive oxygen species signaling and thiol redox regulation in the green lineage. Plant Physiol. *187*, 687–698. https://doi.org/10.1093/plphys/kiab355.

Walters, R.G., Ibrahim, D.G., Horton, P., and Kruger, N.J. (2004). A mutant of Arabidopsis lacking the triose-phosphate/phosphate translocator reveals metabolic regulation of starch breakdown in the light. Plant Physiol. *135*, 891–906. https://doi.org/10.1104/pp.104.040469.

Weber, A.P.M., Linka, M., and Bhattacharya, D. (2006). Single, ancient origin of a plastid metabolite translocator family in Plantae from an endomembrane-derived ancestor. Eukaryot. Cell *5*, 609–612. https://doi.org/10.1128/EC.5.3.609-612.2006.

Winter, H., and Huber, S.C. (2000). Regulation of sucrose metabolism in higher plants: localization and regulation of activity of key enzymes. Crit. Rev. Biochem. Mol. Biol. *35*, 253–289. https://doi.org/10.1080/10409230008984165.

1238 Yoshida, K., and Hisabori, T. (2018). Determining the Rate-Limiting Step for Light-Responsive
1239 Redox Regulation in Chloroplasts. Antioxidants (Basel) *7*. https://doi.org/10.3390/antiox7110153.

1240 Young, J.D., Shastri, A.A., Stephanopoulos, G., and Morgan, J.A. (2011). Mapping
1241 photoautotrophic metabolism with isotopically nonstationary (13)C flux analysis. Metab. Eng. *13*,
1242 656–665. https://doi.org/10.1016/j.ymben.2011.08.002.

1243 Yu, E.T., Zendejas, F.J., Lane, P.D., Gaucher, S., Simmons, B.A., and Lane, T.W. (2009).
1244 Triacylglycerol accumulation and profiling in the model diatoms *Thalassiosira pseudonana* and
1245 *Phaeodactylum tricornutum* (Baccilariophyceae) during starvation. J. Appl. Phycol. *21*, 669–681.
1246 https://doi.org/10.1007/s10811-008-9400-y.

1247 Yu, J., Li, Y., Qin, Z., Guo, S., Li, Y., Miao, Y., Song, C., Chen, S., and Dai, S. (2020). Plant
1248 chloroplast stress response: Insights from thiol redox proteomics. Antioxid. Redox Signal. *33*, 35–
1249 57. https://doi.org/10.1089/ars.2019.7823.

1250 Zhao, Y., Luo, L., Xu, J., Xin, P., Guo, H., Wu, J., Bai, L., Wang, G., Chu, J., Zuo, J., et al. (2018).
1251 Malate transported from chloroplast to mitochondrion triggers production of ROS and PCD in
1252 *Arabidopsis thaliana*. Cell Res. *28*, 448–461. https://doi.org/10.1038/s41422-018-0024-8.

1253 Zhao, Y., Yu, H., Zhou, J.-M., Smith, S.M., and Li, J. (2020). Malate Circulation: Linking
1254 Chloroplast Metabolism to Mitochondrial ROS. Trends Plant Sci. *25*, 446–454.
1255 https://doi.org/10.1016/j.tplants.2020.01.010.

1256 Zimmermann, P., and Zentgraf, U. (2005). The correlation between oxidative stress and leaf
1257 senescence during plant development. Cell. Mol. Biol. Lett. *10*, 515–534. .

1258

1259

1260

1261

1262

1263

1264

1265

1266

1267

1268

1269 **Materials and methods**

1270 **Extraction of samples for LC-MS/MS**

1271 To each cell pellet, 500 µL methanol was added along with internal standards ribitol and PIPES to
1272 a final concentration of 2 µM each. Samples were then vortexed for 30 sec, frozen in liquid
1273 nitrogen as described in (Winder et al. 2008), and allowed to thaw at 0°C. This vortex-freeze-thaw
1274 cycle was repeated twice more before the samples were centrifuged at 10,000 x g at 1°C for 5
1275 minutes. The supernatant was collected, and the remaining pellets were extracted twice more with
1276 500 µL of a 50:50 mixture of methanol and water, with 3 vortex-freeze-thaw cycles done for each
1277 extraction. Supernatants from each extraction procedure were pooled and dried on a Thermo Fisher
1278 SpeedVac Concentrator. Dried extracts were then resuspended in 500 µL water and cleaned to
1279 remove any residual large cell debris by filtration, first through a 0.22 µm pore size Spin-X
1280 centrifugal tube filter, followed by 10 K molecular mass cutoff filters, followed finally by 3 K
1281 molecular mass cutoff filters. After each filtration step, filters were rinsed with 50 µL water, which
1282 was added to the total sample volume for subsequent steps. Filtered extracts were dried again and
1283 resuspended in 200 µL water for LC-MS/MS analysis.

1284 **Analysis of metabolite extracts**

1285 Metabolite extracts were analyzed using an LC-MS/MS method adapted from (Young et al. 2011).
1286 A Phenomenex 150 mm x 2 mm Synergi Hydro-RP column was used on an Agilent 1200 Series
1287 HPLC system coupled to an AB Sciex 5500 QTRAP system. LC was performed with a liquid
1288 injection volume of 20 µL, using gradient elution of 10 mM tributylamine and 15 mM acetic acid
1289 (aqueous phase) and acetonitrile (organic phase) at a constant flow rate of 0.3 mL/min, and a
1290 constant temperature of 40°C. The gradient profile of the organic phase is as follows: 0% B (0
1291 min), 8% B (10 min), 16% B (15 min), 30%B (16.5 min), 30% B (19 min), 90% B (21.5 min), 90%
1292 B (28 min), 0% B (28.5 min), and 0% B (35 min). MS analysis was performed in negative mode
1293 using a multiple reaction monitoring (MRM) acquisition method. Data acquisition was performed
1294 on the ABSciex Analyst 1.7 software. Absolute quantification of intracellular metabolites was
1295 performed using the quantitation mode on the Analyst software.

1296 **Protein extraction and immunoblot analysis**

1297 Affinity-purified polyclonal antibodies to CreTPT3 were custom-made by GenScript. The antigen
1298 sequence used for antibody generation was KSWSFGRPVTKQEF. Chlamydomonas cells were
1299 grown in liquid cultures to 2–5 x10^6 cells ml^{-1} and collected by centrifugation (2700 rpm, 5 min).
1300 Cells were resuspended in resuspension buffer [(5 mM HEPES, pH 7.5, KOH), 10 mM EDTA (pH
1301 7.5, NaOH), 1x protease inhibitor "complete EDTA-free" (Roche)]. For the disruption of cells,
1302 bead-beating was performed using a mini beadbeater (Biospec) in two cycles of 30 sec min^{-1}, with
1303 a 1 min period of cooling on ice between cycles. Disrupted cells were centrifuged at 4°C, 30 min,
1304 14000 rpm in a microfuge. The supernatant was removed, the pellet was resuspended in sample
1305 buffer (resuspension buffer supplemented with 100 mM Na_2CO_3, 100 mM DTT, 2% WT/vol SDS,
1306 and 12% WT /vol sucrose).

1307

1308

1309 SDS-PAGE was performed using a 12% polyacrylamide gel (Bio-Rad), with the electrophoresis
1310 for 90 min at 120 V. Next, proteins were transferred onto a PVDF membrane (Bio-Rad) using
1311 Trans-Blot Turbo (Bio-Rad). The detection was performed using Clarity Max Western ECL
1312 Substrate (Bio-Rad).

1313 **RT-qPCR**

1314 RT-qPCR, was performed as described previously (Kaye et al. 2019). Briefly, total RNA was
1315 isolated using the RNeasy Plant Mini Kit (Qiagen) and treated with DNase I (Qiagen). First-strand
1316 cDNA was generated by reverse transcription of 0.5 µg total RNA using the iScript cDNA
1317 Synthesis Kit (Bio-Rad). Real-time PCR using the Roche Light Cycler 480 was performed with
1318 the SensiMix NO-Rox SYBR Green I Kit as described by the manufacturer (Bioline). Oligos used
1319 in this research for analyzing the expression levels of *CreTPT1/2/3/25* are listed in **Supplemental**
1320 **Table 1**.

1321 **Analysis of transcript levels in response to different conditions**

1322 In order to analyze the transcript level of Cre*TPT* genes under different conditions, we obtained
1323 RNAseq data published previously in which cells experienced a diurnal cycle, nitrogen starvation,
1324 sulfur starvation and Fe^{2+} starvation (Strenkert et al. 2019; Zones et al. 2015; Ngan et al. 2015;
1325 González-Ballester et al. 2010; Urzica et al. 2013). The log2 fold change of each gene was
1326 calculated based on the ratio of transcript abundance at different time point over transcript level at
1327 time point 0 h. The fold change was visualized by a heatmap and the color bar is the scale of log2
1328 (fold-change).

1329 **In vivo polymeric carbohydrate staining**

1330 Lugol's iodine (aqueous solution of 1.8% iodine and 3.0% potassium iodide) was used to stain in
1331 vivo polymeric carbohydrate. Briefly, 0.5 mL of the cell culture was pelleted, resuspended in 10
1332 µL of Lugol's iodine and visualized under a bright-field microscope. Lugol's iodine selectively
1333 binds to alpha-1,4 glucans and stains it blue-black.

1334 **References**

1335 González-Ballester, David, David Casero, Shawn Cokus, Matteo Pellegrini, Sabeeha S. Merchant,
1336 and Arthur R. Grossman. 2010. "RNA-Seq Analysis of Sulfur-Deprived Chlamydomonas Cells
1337 Reveals Aspects of Acclimation Critical for Cell Survival." *The Plant Cell* 22 (6): 2058–84.

1338 Kaye, Yuval, Weichao Huang, Sophie Clowez, Shai Saroussi, Adam Idoine, Emanuel Sanz-Luque,
1339 and Arthur R. Grossman. 2019. "The Mitochondrial Alternative Oxidase from *Chlamydomonas*
1340 *reinhardtii* Enables Survival in High Light." *The Journal of Biological Chemistry* 294 (4): 1380–
1341 95.

1342 Ngan, Chew Yee, Chee-Hong Wong, Cindy Choi, Yuko Yoshinaga, Katherine Louie, Jing Jia,
1343 Cindy Chen, et al. 2015. "Lineage-Specific Chromatin Signatures Reveal a Regulator of Lipid
1344 Metabolism in Microalgae." *Nature Plants* 1 (8): 15107.

1345 Strenkert, Daniela, Stefan Schmollinger, Sean D. Gallaher, Patrice A. Salomé, Samuel O. Purvine,

Carrie D. Nicora, Tabea Mettler-Altmann, et al. 2019. "Multiomics Resolution of Molecular Events during a Day in the Life of Chlamydomonas." *Proceedings of the National Academy of Sciences of the United States of America* 116 (6): 2374–83.

Urzica, Eugen I., Astrid Vieler, Anne Hong-Hermesdorf, M. Dudley Page, David Casero, Sean D. Gallaher, Janette Kropat, Matteo Pellegrini, Christoph Benning, and Sabeeha S. Merchant. 2013. "Remodeling of Membrane Lipids in Iron-Starved Chlamydomonas." *The Journal of Biological Chemistry* 288 (42): 30246–58.

Winder, Catherine L., Warwick B. Dunn, Stephanie Schuler, David Broadhurst, Roger Jarvis, Gillian M. Stephens, and Royston Goodacre. 2008. "Global Metabolic Profiling of Escherichia Coli Cultures: An Evaluation of Methods for Quenching and Extraction of Intracellular Metabolites." *Analytical Chemistry* 80 (8): 2939–48.

Young, Jamey D., Avantika A. Shastri, Gregory Stephanopoulos, and John A. Morgan. 2011. "Mapping Photoautotrophic Metabolism with Isotopically Nonstationary (13)C Flux Analysis." *Metabolic Engineering* 13 (6): 656–65.

Zones, James Matt, Ian K. Blaby, Sabeeha S. Merchant, and James G. Umen. 2015. "High-Resolution Profiling of a Synchronized Diurnal Transcriptome from *Chlamydomonas reinhardtii* Reveals Continuous Cell and Metabolic Differentiation." *The Plant Cell* 27 (10): 2743–69.

oligo name	sequence
gTPT3_pRam118_f	tactcacaacaagcccagttATGGCTTCGCTCGCTCAGCGCGTGAGC
gTPT3_pRam118_r	agcggggatccttatccgttTTAGGCCGCGGCCGGCGACGC
TPT3pro1000_f	gccttttgctcacatgtggcggccgccgccatgctggccaacag
TPT3pro1000_r	taccaatccacaaatgtgggctagcccatgtgaaggcgttgacc
TPT3_3UTR_f	gatgacgacaagtaaagatctTAAGGCGGGCAGCGGC
TPT3_3UTR_r	GCGCAAGAAAGAAGCTTGATATCCCCCTTATAATGTTTACAAGTGGTGCG
hygro_crispr_f2	GGAACTGGCGCAGTTCCTCTG
hygro_crispr_re2	GGCTCGCGTAGGAATCATCCG
TPT3_gRNA1_F	GCTCGGTTGAGCGCACCC
TPT3_gRNA1_R	CAAGGGTCTGGCGAGCACG
TPT3_gRNA2_F	ACCTCCCCATCGCCACGAT
TPT3_gRNA2_R	AGGGGTAAGGACAGCGGTG
Qrt_TPT1_f2	CCTGTACCAGCAGGTGTCGTAC
Qrt_TPT1_r2	CCAGCGCGTTCTGGAGTGACA
Qrt_TPT2_f2	ATGGCGTCTCTGCTGGGC
Qrt_TPT2_r2	CTGCTCGCCCATTCTCCTC
Qrt_TPT3_f2	GCAAAGCTGGCGCCTACTG
Qrt_TPT3_r2	TAGACCAGGCCGACCACCAC
Qrt_TPT25_f1	CTGGTTCATCGGGACATGGC
Qrt_TPT25_r1	TGGCTGAAGCTGACCACT

Supplementary Table 1: oligo list.

Cre ID	Name	Prediction	CS Position
Cre08.g379350.t1.1	CreTPT1	cTP	CS pos: 61-62. TCL-AV.
Cre06.g263850.t1.1	CreTPT2	cTP	CS pos: 70-71. VCQ-AA.
Cre01.g045550.t1.2	CreTPT3	cTP	CS pos: 60-61. VTK-AS.
Cre02.g106200.t1.2	CreTPT4	OTHER	
Cre02.g112900.t1.2	CreTPT5	OTHER	
Cre02.g144300.t1.2	CreTPT6	OTHER	
Cre03.g162000.t1.2	CreTPT7	OTHER	
Cre03.g184850.t1.1	CreTPT8	OTHER	
Cre04.g227450.t1.2	CreTPT9	OTHER	
Cre07.g330850.t1.1	CreTPT10	OTHER	
Cre08.g363600.t1.2	CreTPT11	OTHER	
Cre09.g408400.t1.1	CreTPT12	OTHER	
Cre09.g413700.t1.1	CreTPT13	OTHER	
Cre08.g382350.t1.2	CreTPT14	OTHER	
Cre09.g415900.t1.2	CreTPT15	OTHER	
Cre10.g452750.t1.2	CreTPT16	OTHER	
Cre11.g479950.t1.2	CreTPT17	OTHER	
Cre12.g490050.t1.2	CreTPT18	OTHER	
Cre12.g490100.t1.2	CreTPT19	OTHER	
Cre12.g501000.t1.1	CreTPT20	OTHER	
Cre15.g641266.t1.1	CreTPT22	OTHER	
Cre15.g642950.t1.2	CreTPT23	OTHER	
Cre15.g643385.t1.1	CreTPT24	OTHER	
Cre16.g663800.t1.2	CreTPT25	cTP	CS pos: 70-71. IVA-SS.
Cre16.g666250.t1.2	CreTPT26	OTHER	
Cre17.g702700.t1.1	CreTPT27	OTHER	
Cre17.g703250.t1.2	CreTPT28	OTHER	
Cre17.g710850.t1.2	CreTPT29	OTHER	
Cre11.g467754.t1.1	CreTPT30	OTHER	
Cre14.g622700.t1.2	CreTPT31	OTHER	
Cre18.g748947.t1.1	CreTPT32	OTHER	
Cre09.g408428.t1.2	CreTPT33	OTHER	

Supplementary Table 2: Members of the triose phosphate transporter family in *Chlamydomonas reinhardtii* and their predicted subcellular localization based on TargetP-2.0. cTP, chloroplast transit peptide; CS position, transit peptides cleavage site.

Name	D_11h	D_9h	D_7h	D_5h	D_3h	D_1h	D_0.5h	D_0h	L_0.5h	L_1h	L_3h	L_5h	L_7h	L_9h	L_11h	D_13h
TPT1	5.2883	10.2702	9.45732	8.85549	7.70518	6.18466	7.5509	9.07019	0.511726	0.198621	0.329098	1.99425	2.93498	2.13736	1.02291	9.56813
TPT2	6.46543	9.45107	9.77461	10.5338	12.8513	8.72194	9.51834	10.275	59.1606	62.7836	33.5533	12.891	5.69013	5.94982	12.1866	3.6131
TPT3	233.805	337.793	247.287	181.496	131.602	97.1854	105.57	98.3637	71.9013	43.1935	218.026	280.947	185.973	179.459	157.828	312.135
TPT25	38.9867	62.7835	45.3561	32.7872	22.8554	14.8691	15.5851	13.8916	19.6257	26.8661	10.2213	7.48595	8.11458	19.7874	32.0979	53.4145

Supplemental Table S3: Expression levels of TPTs predicted on the chloroplast envelope over the diel cycle in Chlamydomonas. Data were extracted from (Strenkert et al. 2019).

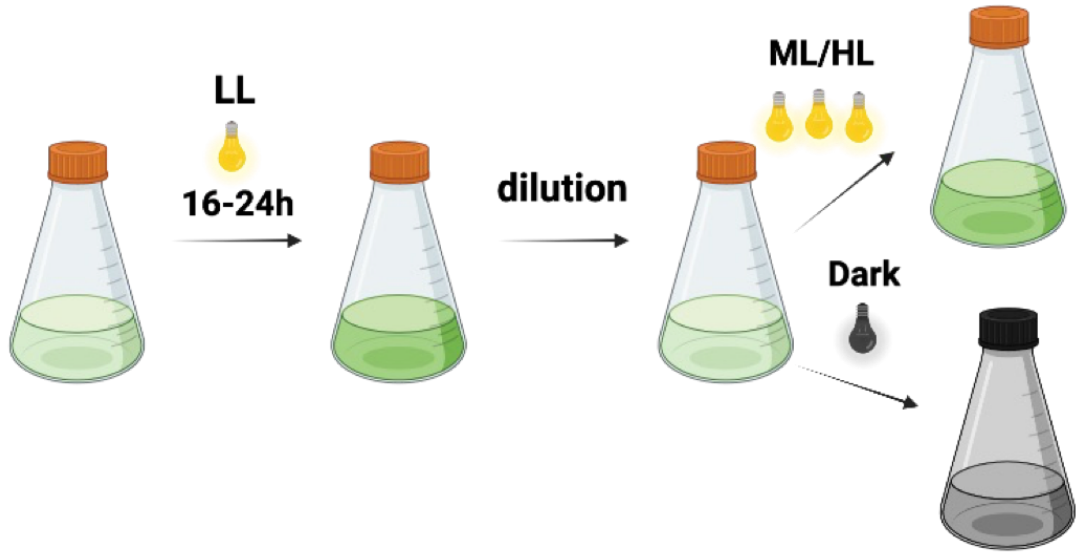

1388
1389 **Supplementary Fig. 1: Experimental set up.** All strains were grown photoautotrophically under
1390 low white light (~30 µmol photons m^{-2} s^{-1}, LL) for 16-24 h. After dilution with fresh medium, the
1391 cultures were transferred to moderate light (250-300 µmol photon m^{-2} s^{-1}, ML). On occasion, the
1392 cultures were also transferred to the dark or high light (~450 µmol photon $m^{-2}s^{-1}$) for 24 or 48 h.
1393 To avoid self-shading, the culture density was adjusted to 1-1.5 µg/mL chlorophyll before
1394 exposure to ML or HL.

1395

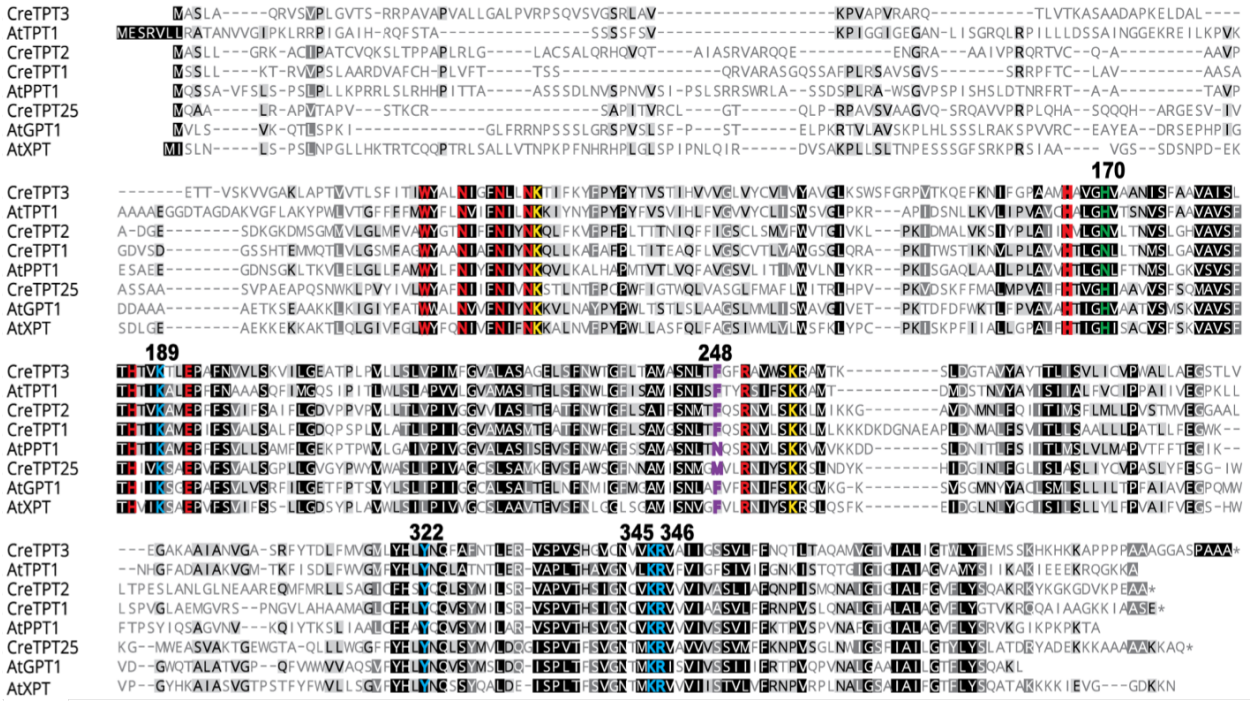

Supplementary Fig. 2: Sequence alignment of the plastid phosphate transporter sequences of *Arabidopsis thaliana* and *Chlamydomonas reinhardtii.* Plastid TPTs from Chlamydomonas are CreTPT1 (Cre08.g379350.t1.1), CreTPT2 (Cre06.g263850.t1.1), CreTPT3 (Cre01.g045550.t1.2), and CreTPT25 (Cre16.g663800.t1.2). Sequences from *Arabidopsis thaliana* are AtTPT1 (AT5G46110.1), AtPPT1 (AT5G33320.1), AtGPT1 (AT5G54800.1) and AtXPT1 (AT5G17630.1). Conserved substrate binding pockets are colored red. Phosphate-binding residues are highlighted with blue. The gate capping residues are marked with yellow. The positions of residue in green are crucial for the preference of triose-phosphate or 3-PGA. The positions of purple residues are critical for the specificity of PEP.

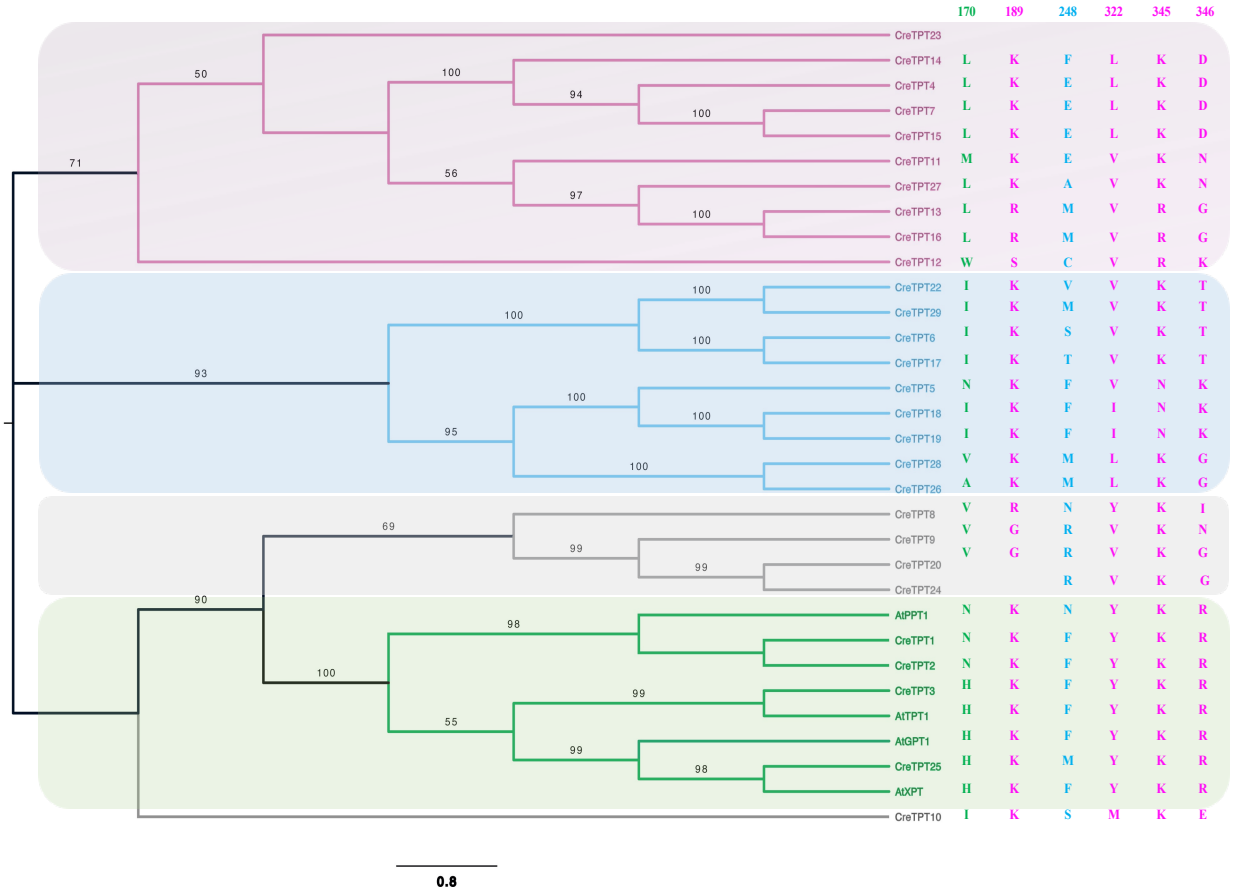

Supplementary Fig. 3: Phylogeny of TPT homologues in Chlamydomonas. Amino acid residues at the positions responsible for substrate specificity in TPT homologues are listed. The numbers above the amino acids are the position of each residue in CreTPT3. The residues marked with green, blue and purple colors are crucial for the preference of triose-phosphate or 3-PGA, for the specificity of PEP and for the binding of phosphate, respectively. Plastid PPT, XPT, and TPT from *Arabidopsis thaliana* are included in the analysis.

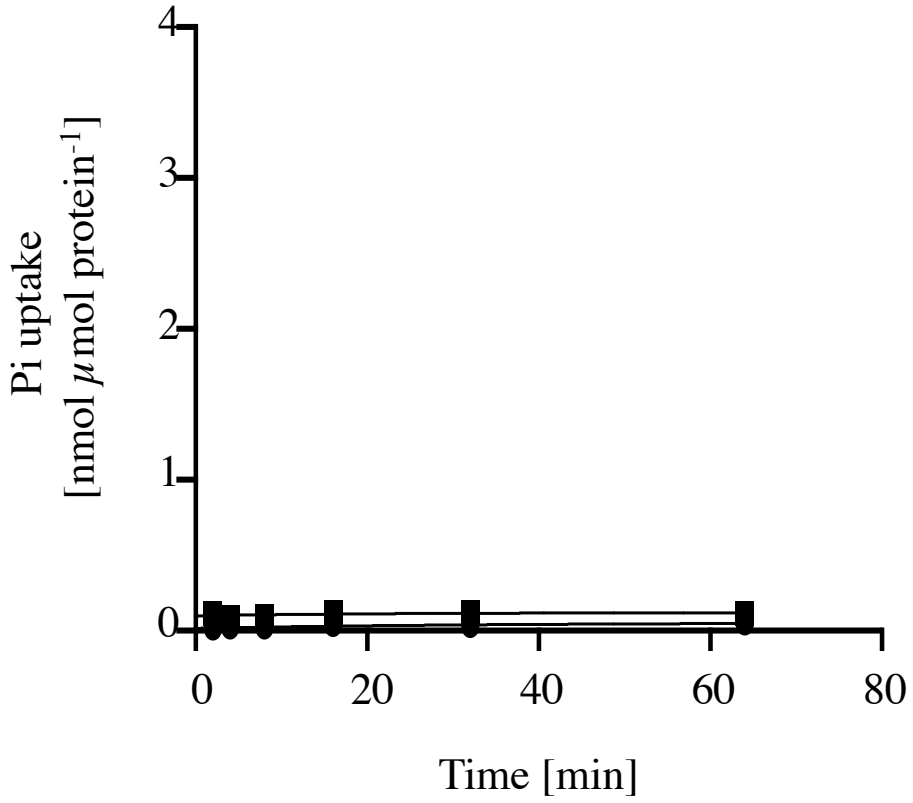

1415

1416 **Supplementary Fig. 4: Background activity of Pi uptake derived from endogenous yeast**
1417 **transporter reconstituted into liposomes.** Time-dependent uptake of Pi (0.25 mM) into
1418 reconstituted liposomes preloaded with 30 mM of Pi (■) or without exchange substrate (●)
1419 prepared from yeast cells harboring the empty vector (pYES-NTa). The arithmetic mean (±SD) of
1420 three independent experiments (each with three technical replicates) was plotted against time. The
1421 observed Pi uptake rates of endogenous yeast carrier reconstituted into liposomes were negligible
1422 compared to the rates of His-CreTPT3 (20-fold higher, **Fig. 1d**), indicating that this expression
1423 system is suitable for functional analysis of recombinant phosphate transporters.

1424

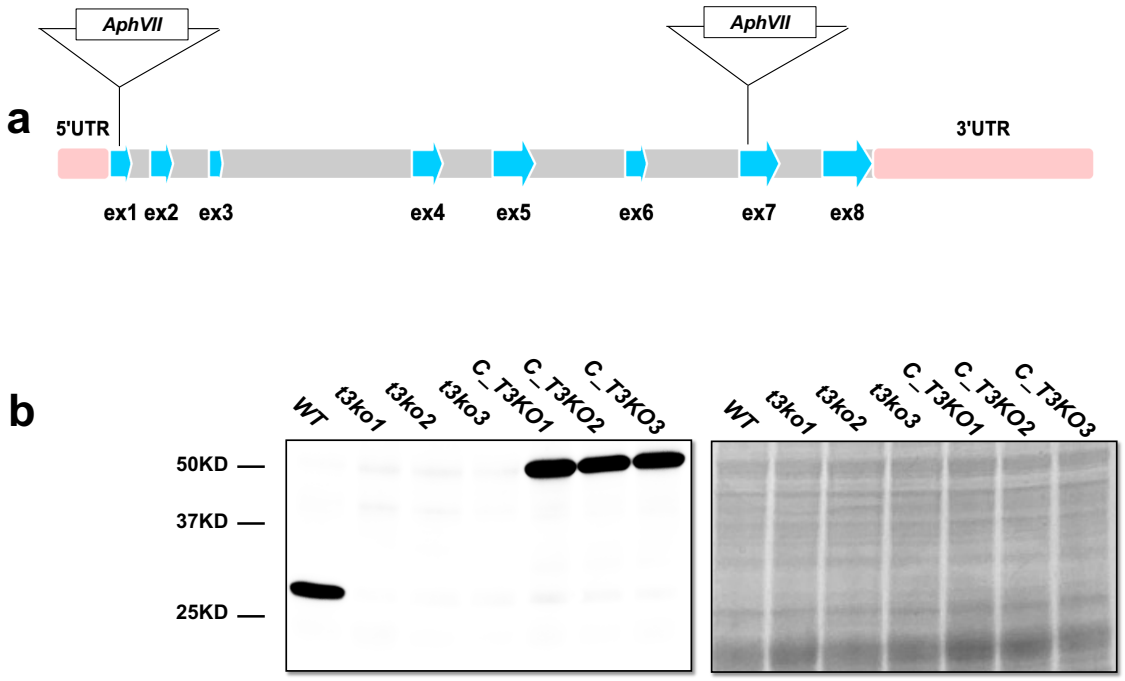

1425

1426 **Supplementary Fig. 5: Inactivation of Cre*TPT3* by CRISPR-Cas9.** (**a**) Molecular map of
1427 Cre*TPT3* gene and positions of the Cas9 targeted sites. The edited sites are located in exons 1 and
1428 7; *t3ko1* has the marker gene inserted in exon 1 and *t3ko2* and *t3ko3* has the marker gene inserted
1429 in exon 7. (**b**) Western blot (left) and loading control (right) of wild type, *t3ko1*, *t3ko2*, *t3ko3* and
1430 the complemented strains (C_T3KO1, C_T3KO2 and C_T3KO3, respectively).

1431

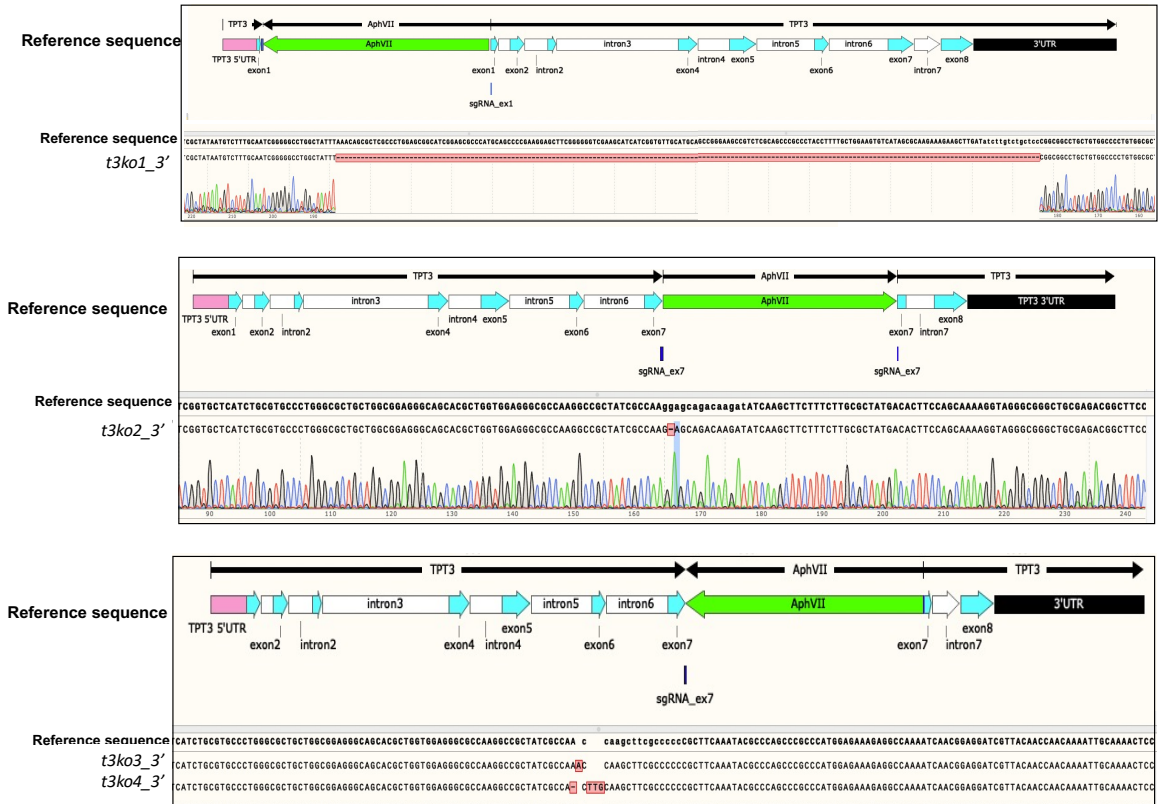

Supplementary Fig. 6: Sequencing of genomic DNA fragments across the site of insertion of the drug resistant marker (*AphVII* cassette, which confers hygromycin resistance) in the different *tpt3* mutants (*t3ko1*, *t3ko2*, *t3ko3* and *t3ko4*).

1437

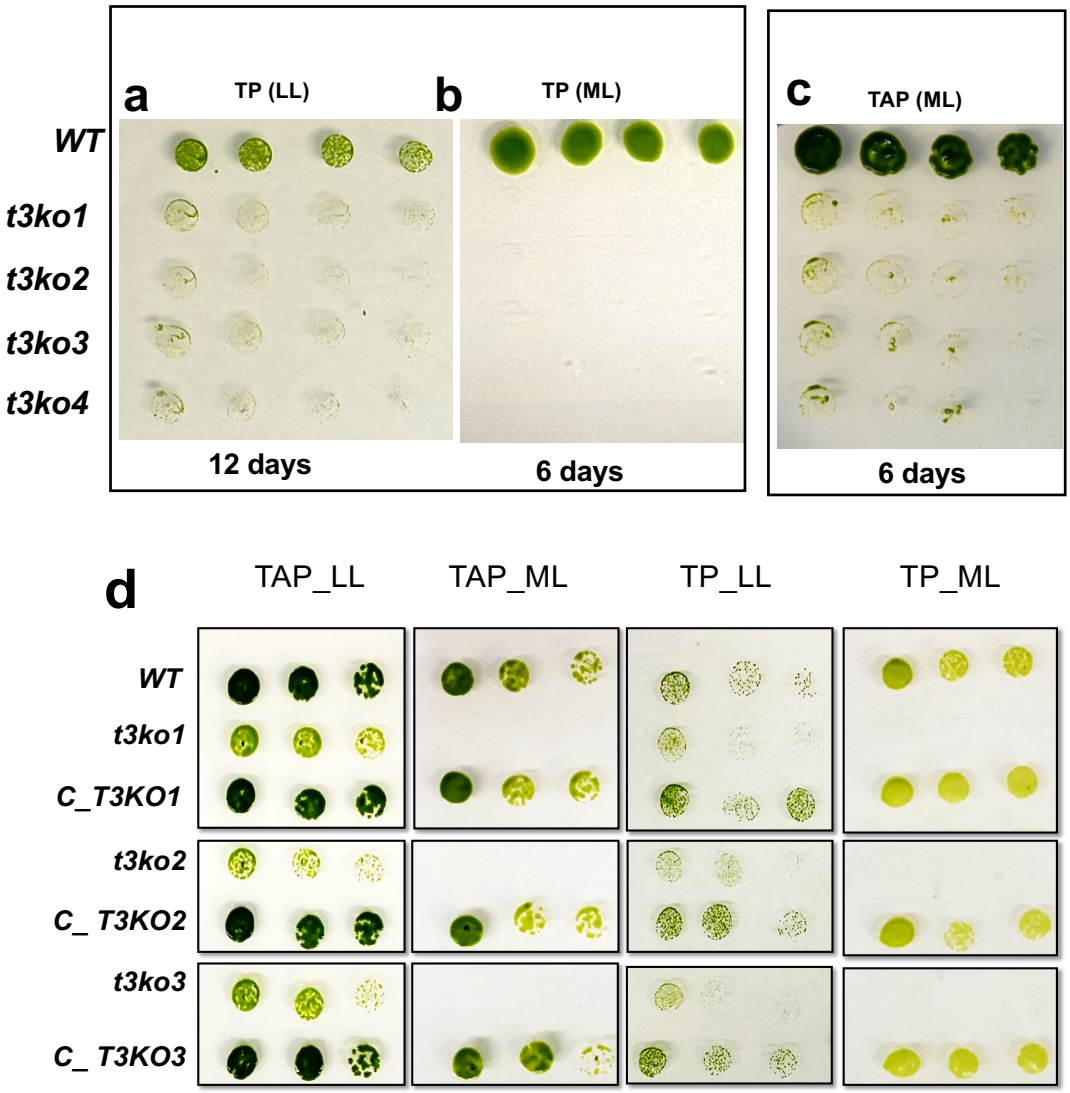

1438

1439 **Supplementary Fig. 7: Growth of the CRISPR-Cas9 generated Cre*tpt3* mutants on solid**
1440 **medium.** (**a**) Cells were spotted on plates containing TP medium under continuous LL or (**b**) ML.
1441 (**c**) Cells were spotted on agar plates containing TAP medium under continuous ML. The dilution
1442 series from (**a**,**b**,**c**) were 2.0, 0.75, 0.375 µg/mL chlorophyll. (**d**) Growth of wild type (WT), *t3ko1*,
1443 *t3ko2*, *t3ko3* and the complemented strains on agar plates containing TAP or TP medium under
1444 LL or ML for 4 d. The dilution series used was 1.5, 0.75, 0.375 µg/mL chlorophyll.

1445

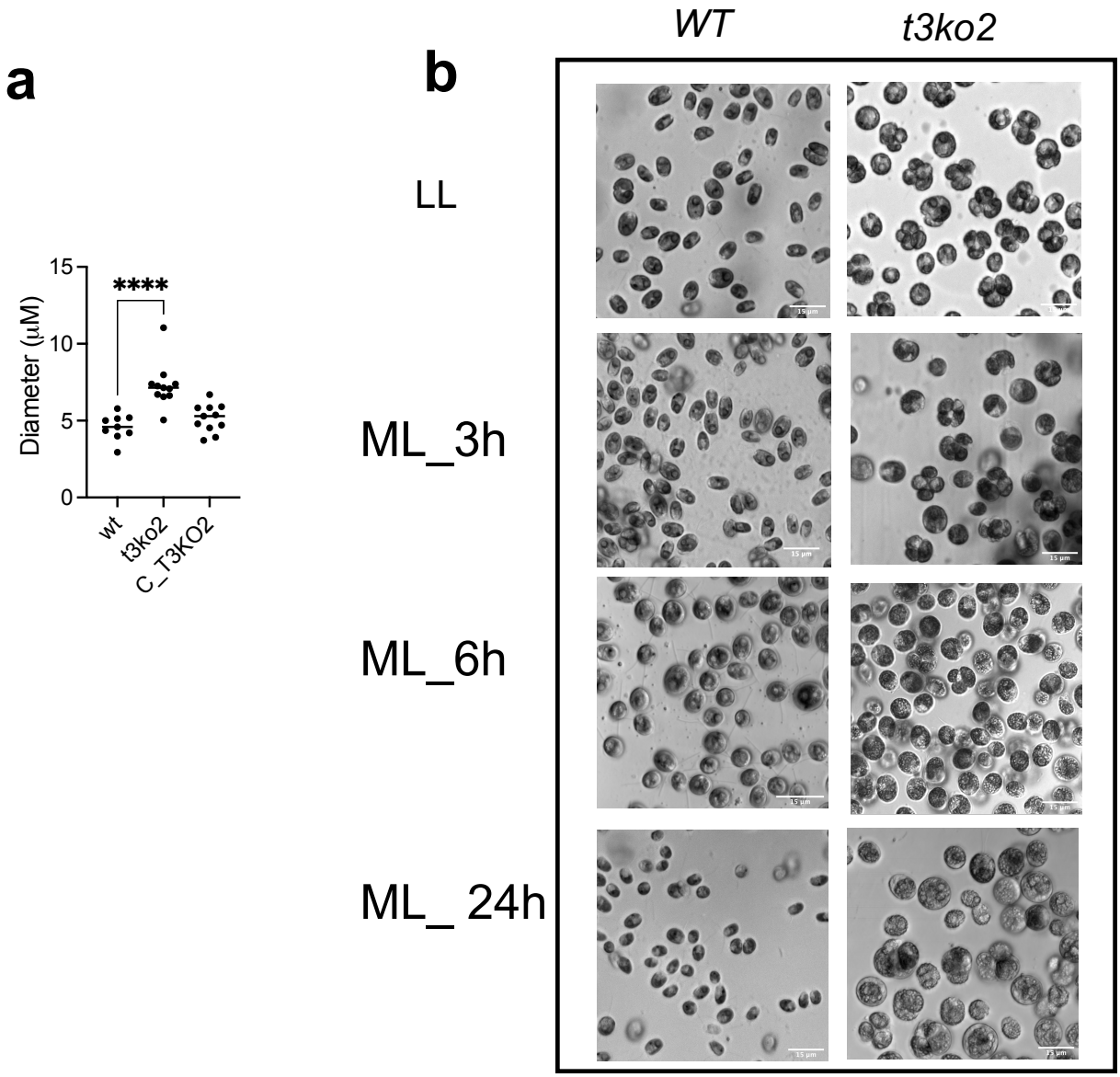

Supplementary Fig. 8: (a) Cell size of WT, *t3ko2*, and C_T3KO2 in TP under both LL and ML. **(b)** WT and *t3ko2* morphology changes following a LL to ML transition.

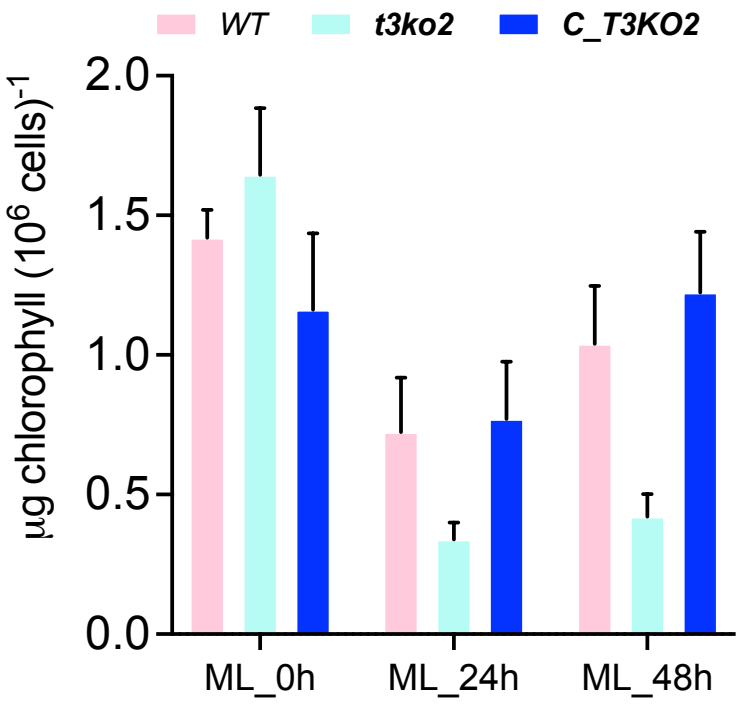

1450

1451 **Supplementary Fig. 9: Loss of chlorophyll. Quantification of chlorophyll contents in**
1452 **indicated strains after exposure to ML for 24 and 48 h.** All strains were grown
1453 photoautotrophically under LL (~30 µmol photons m^{-2} s^{-1}) for 16-24 h. After dilution with fresh
1454 medium, the culture was transferred to ML for over 24 h. The initial inoculum density used for the
1455 transition was between 1-1.5 µg/mL chlorophyll in order to avoid self-shading.

1456

1457

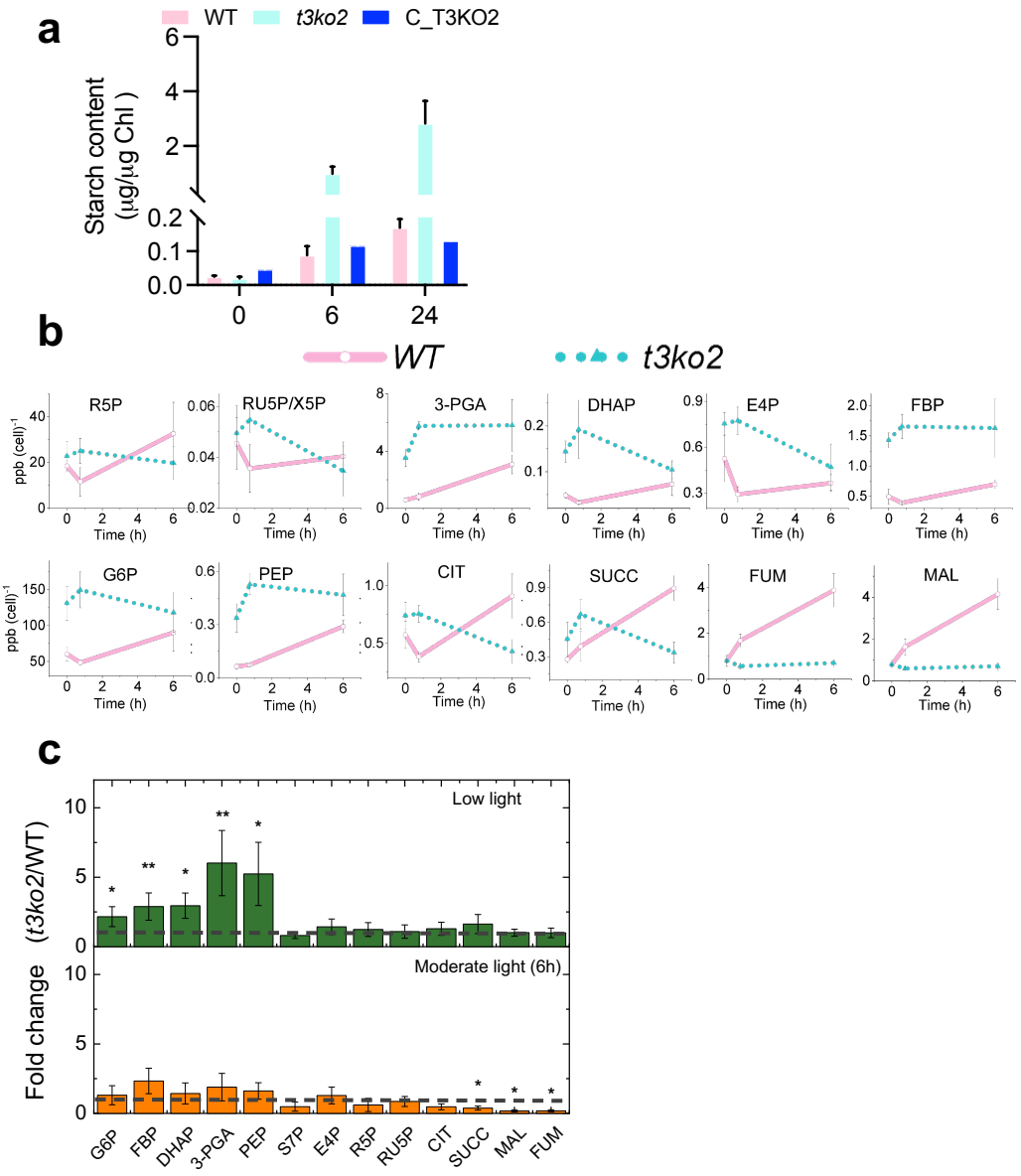

Supplementary Fig. 10: (**a**) Starch contents in indicated strains following 0, 6, and 24 h of LL exposure in TP. (**b**) Time course of change in the metabolite pool sizes at 0 h (LL), 45 min and 6 h after shifting LL-grown cells to ML. Data was normalized to cell numbers. (**c**) Schematic representation of the fold-change for the metabolites shown in (**b**), calculated by dividing the pool size in *t3ko2* by that of WT cells under the same conditions. Fold change of 1 (no change) is shown by a dashed line. Each data point is the mean and standard error of three biological replicates. Asterisk indicates statistically significant differences relative to WT (* P<0.05, ** P<0.01, *** P<0.001). Abbreviations: G6P, glucose-6-phosphate; FBP, fructose bisphosphate; DHAP, dihydroxyacetone phosphate; 3-PGA, 3-phosphoglycerate; PEP, phosphoenolpyruvate; CIT, citrate; SUCC, succinate; FUM, fumarate; MAL, malate; S7P, sedoheptulose-7-phosphate; E4P, Erythrose 4-phosphate; R5P, Ribose 5-phosphate; RU5P/X5P, ribulose 5-phosphate/xylulose-5-phosphate;

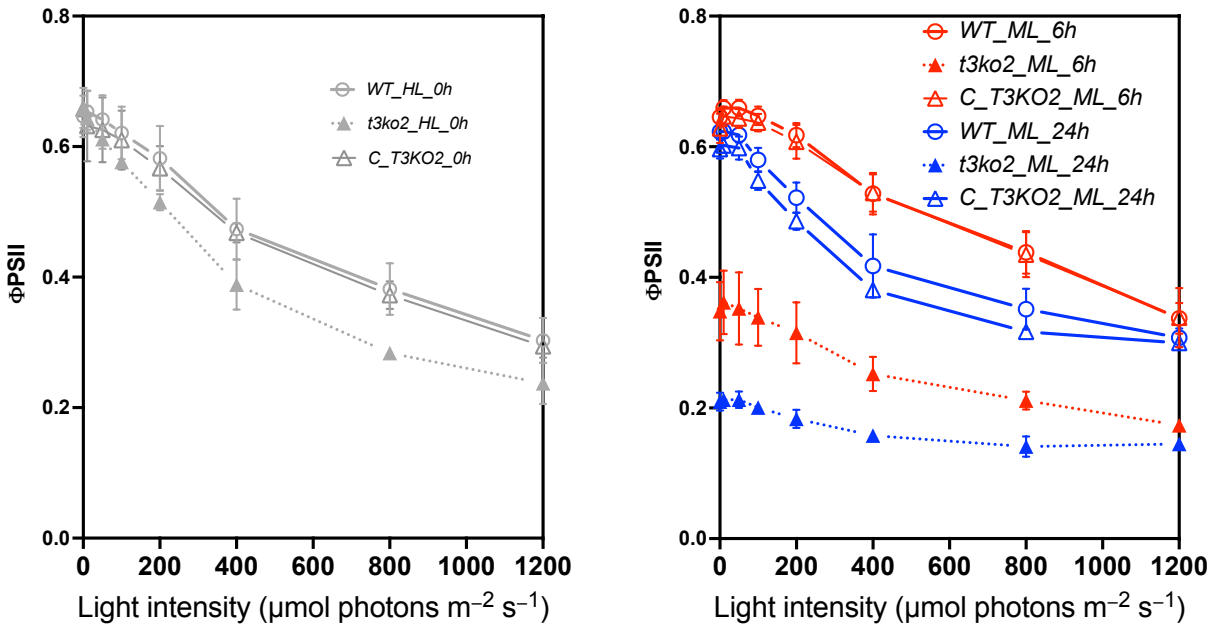

Supplementary Fig. 11: Quantum yield of PSII (ΦPSII) grown in LL (0 h: left) and after 6 and 24 h in ML (right) following exposure to increasing actinic light intensities.

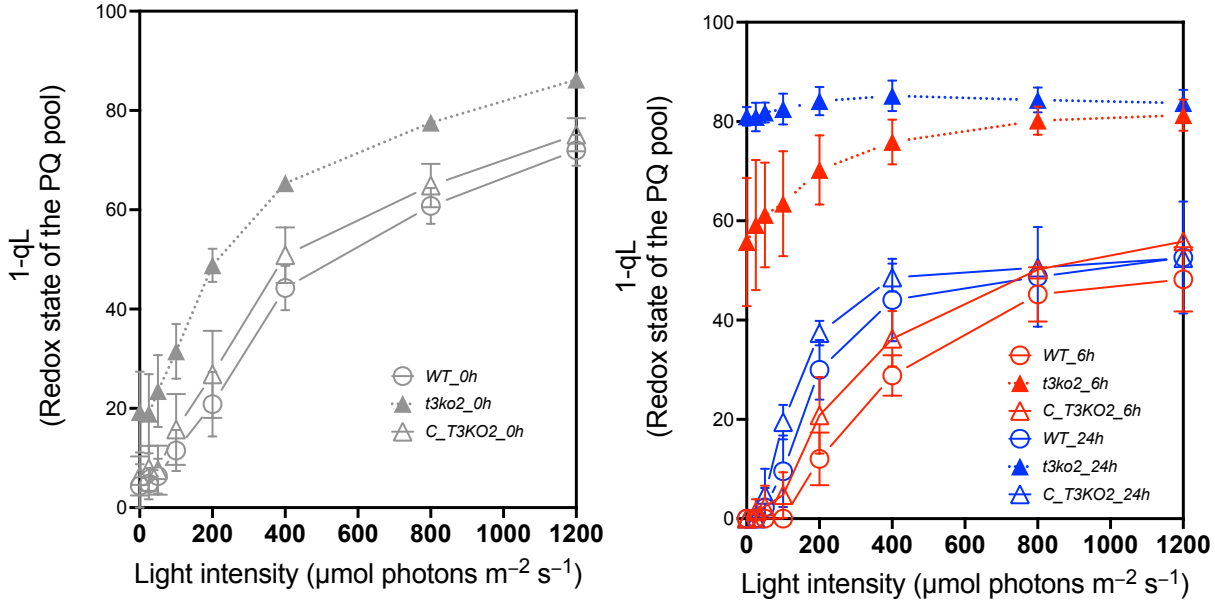

Supplementary Fig. 12: Redox state of the PQ pool followed by LL to ML transition. 1-qL values of LL (left) and ML (right) acclimated cells exposed to increasing light intensities.

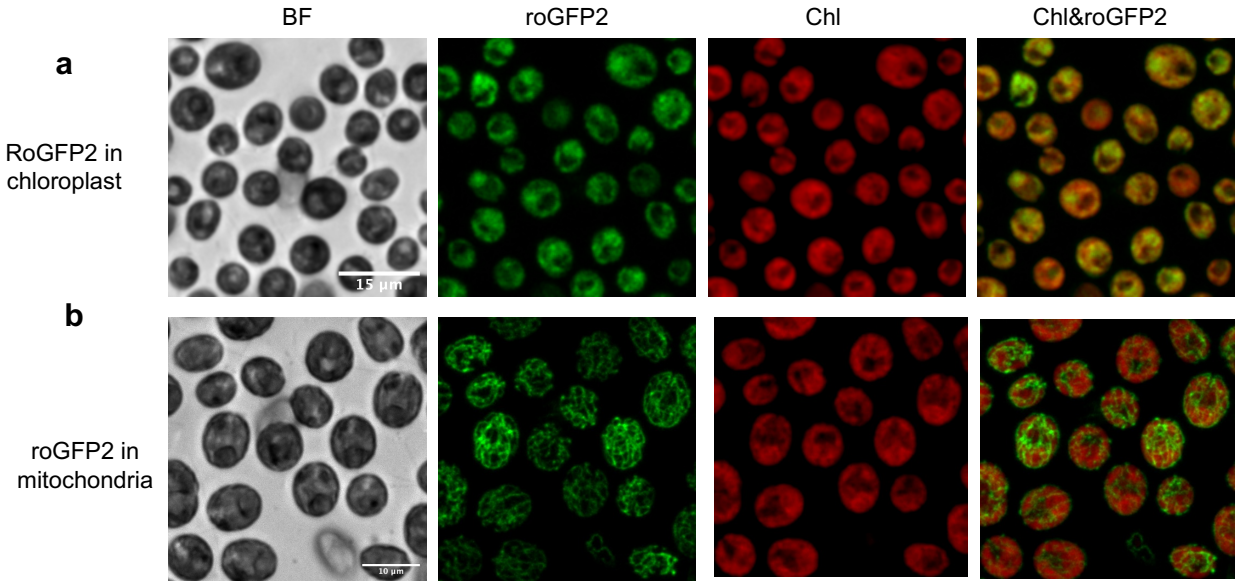

1480

1481 **Supplementary Fig. 13:** Redox-sensitive GFP (roGFP) protein was targeted to the chloroplast (**a**)
1482 and mitochondrion (**b**). BF: bright field; roGFP2 fluorescence: green; Chlorophyll (Chl)
1483 autofluorescence: red.

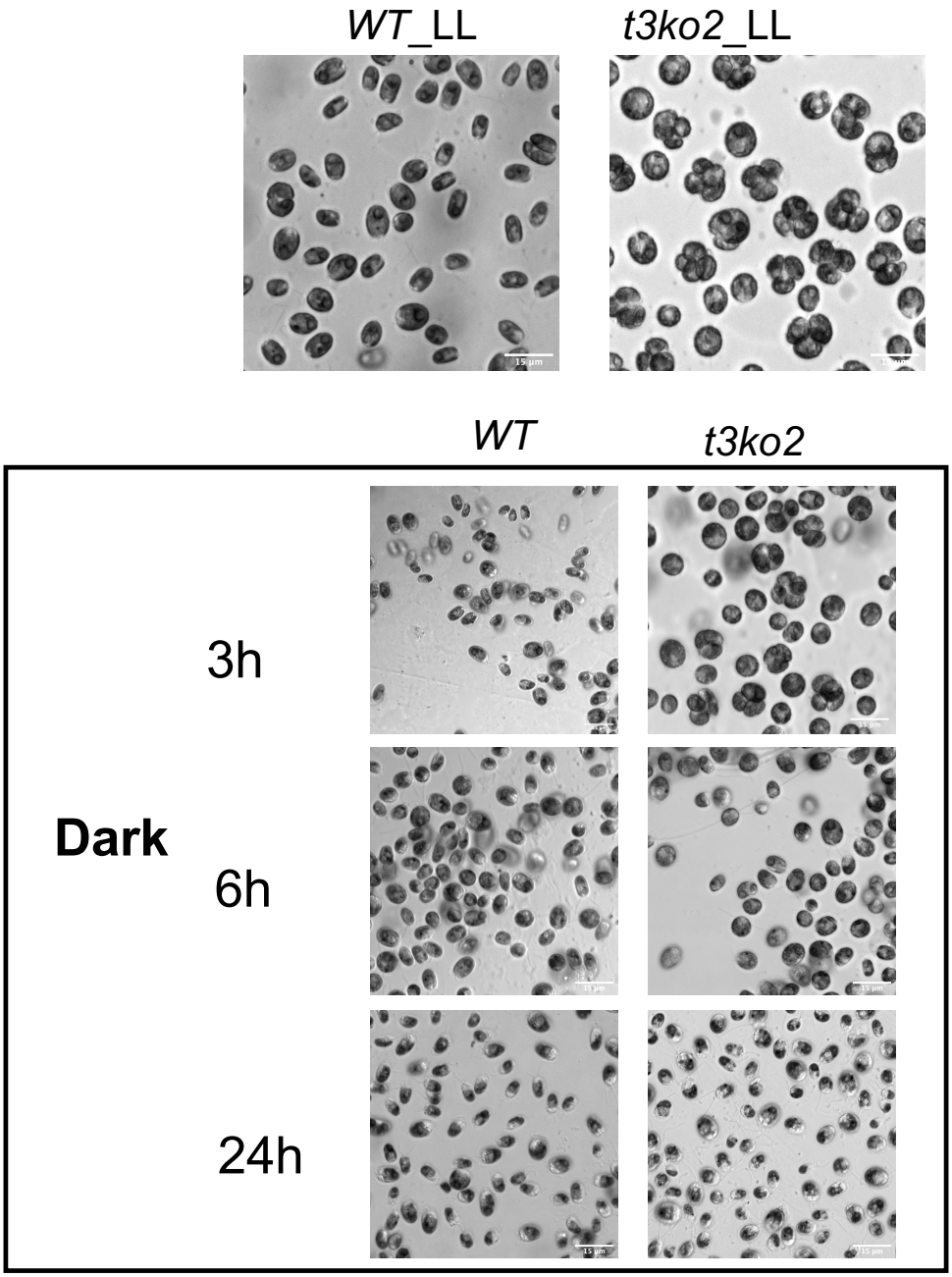

Supplementary Fig. 14: WT and *t3ko2* morphology changes followed by a LL (~30 µmol photons m^{-2} s^{-1}) to dark transition.

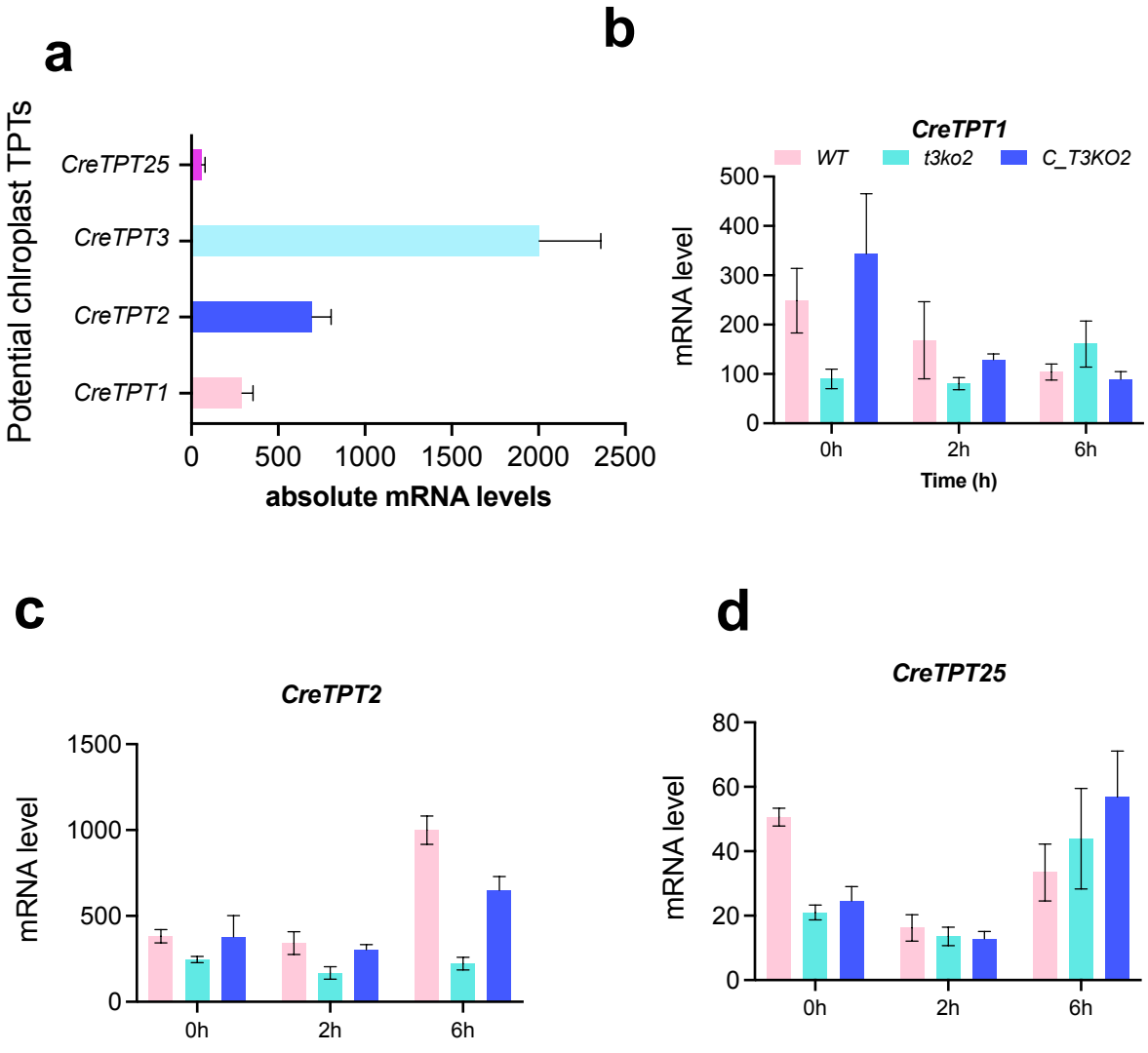

Supplementary Fig. 15: (**a**) mRNA levels of TPTs predicted to be on the chloroplast envelope under LL during growth in TP medium. mRNA levels of CreTPT1 (**b**), CreTPT2 (**c**) and CreTPT25 (**d**) in the indicated strains 0, 2, 4 h after the cells were shifted from LL to ML.

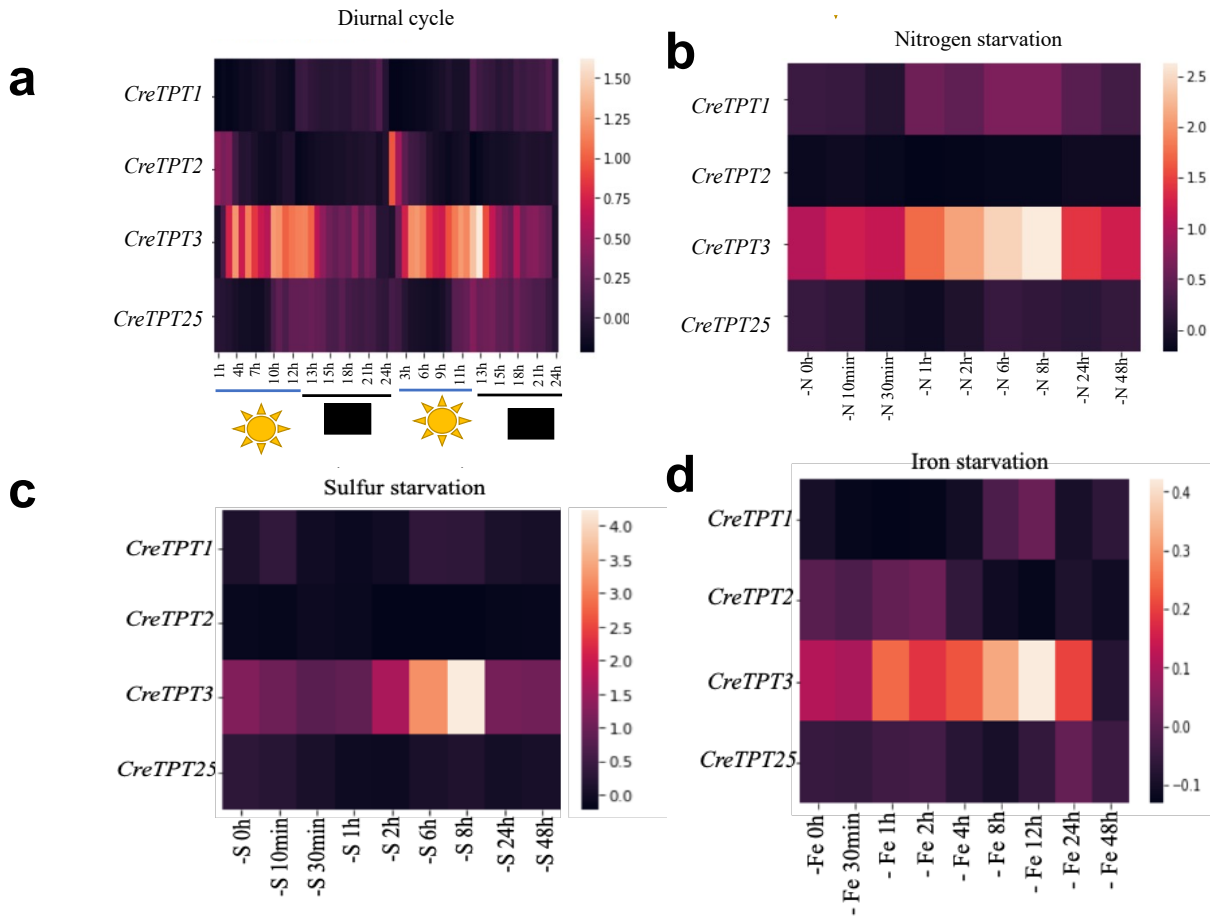

Supplementary Fig. 16: Expression of chloroplast Chlamydomonas TPTs under diurnal cycle (**a**), nitrogen starvation (**b**), sulfur starvation (**c**), and (**d**) iron starvation (Zones et al. 2015; Ngan et al. 2015; González-Ballester et al. 2010; Urzica et al. 2013).